Quantum State Tomography

of the 6 qubit photonic symmetric Dicke State

Alexander Niggebaum

München 2011

Quantum State Tomography

of the 6 qubit photonic symmetric Dicke State

Alexander Niggebaum

Masterarbeit
an der Fakultät für Physik
der Ludwig–Maximilians–Universität
München

vorgelegt von
Alexander Niggebaum
aus Fürstenfeldbruck

München, den 27.10.2011

Written in the group of Prof. Dr. Harald Weinfurter

Contents

Nomenclature

APD	Avalanche Photo Diode
BBO	β-Barium-Borate. Crystal material used to create entangled photons in Spontaneous Parametric Down Conversion (SPDC)
CW	Continuous Wave (Laser)
FPGA	Field Programmable Gate Array
HWP	Half Wave Plate or $\frac{\lambda}{2}$ plate
LBO	Lithium Triborate. Crystal used for upconversion.
MLE	Maximum Likelihood Estimation
PBS	Polarizing Beam Splitter
PI	Permutationally Invariant
QWP	Quarter Wave Plate or $\frac{\lambda}{4}$ plate
SPDC	Spontaneous Parametric Down Conversion

1 Introduction

Entanglement of particles or systems has been widely investigated in recent years[15, 25, 42]. Small 2 qubit systems are easy to produce and observe. Entanglement itself becomes visible if the system is well isolated from external influences. Otherwise interaction with the environment will lead to what is called decoherence and is the generic term for quantum members loosing coherency by interaction with other systems that are not part of the investigation. Thus isolation is crucial. In case of atoms this can be done in magneto optical traps[30] where counter propagating laser beams along the generic three dimensional axes in combination with a magnetic filed gradient are used. Experimental requirements are in general very high[36]. A convenient system consists of photons because of no effective interaction among each other and easy production in large quantities. Any quantum state however is destroyed during a measurement because the photon must be absorbed in the active material of the detector to generate an electric pulse. There are schemes that demonstrate the realization of quantum non demolition measurements on photons[32] but performance is still not optimal compared to destructive methods. If the state is not subject to reutilization, standard techniques suffice.

A problem with larger systems is the increasing number of parameters needed to describe it. Full information include relations between every member with each other. To measure the state of a system, generic schemes were developed[22]. For reliable information of every parameter in the system, sufficient amount of data need to be collected, so the overall measurement time increases as well. In addition, most multiqubit states are either hard to create or store, so measurement time must be kept as short and effective as possible. In this thesis the general tomographic scheme for qubit quantum systems will be introduced. In a bright laser system the Symmetric Dicke State[11] consisting of 6 photonic qubits, each entangled with every other, can be created and observed. Experimental conditions impose low production rates that render the generic approach impossible.

Permutational invariant state tomography, a scheme that exploits the symmetry of the state is used to reduce the amount of data needed for reconstruction. Time and amount of data can be reduced by 96.2% while still reproducing full information on the state. An a priori check ensures that the state follows the necessary symmetry. Gathered data can be reused in the later process. This makes permutational invariant tomography highly effective on symmetric states.

2 State description in quantum mechanics

In this work, experimental creation and observation of a genuine 6 partite entangled state are described. The basic framework to describe quantum mechanical states will be summarized in this chapter. In addition, basic measures used to compare measured with theoretically expected states are motivated. The choice of topics relies on aspects needed for the later description of the experiment; in depth derivation and also motivation of the mathematical framework of quantum mechanics are presented in textbooks, e.g. [34, 18, 12, 38].

2.1 Quantum mechanical states

In analogy to the basic unit of information in computer science, the state of a quantum system is called a "quantum bit" or short "qubit", as coined by Schumacher[37]. Like its digital analogue it is a 2 level system that can be in the *excited* or *unexcited* state. Implementations can vary, dependent the carrier system chosen[1]. Basic requirement for all is long time stability to perform operations with the bits or even store them. Some systems are better suited to meet this prerequisite, other require great experimental effort (e.g. trapped ions).

In contrast to a bit, a qubit can exist in superposition of its two states. However a single readout will show it to be in either one state. Consecutive measurements will map the superposition on the recorded statistics[2], but the individual outcome is not predictable. For their nonexistent interaction with each other and easy experimental implementation, photons are used here. We define horizontal polarization as the excited $|\mathrm{H}\rangle$ and vertical polarization $|\mathrm{V}\rangle$ as the unexcited state. The general superposition reads

$$|\psi\rangle = \cos\left(\frac{\theta}{2}\right)|\mathrm{H}\rangle + e^{i\phi}\sin\left(\frac{\theta}{2}\right)|\mathrm{V}\rangle$$

[1] For example ions use metastable atom levels and superconducting qubits the flux quantization of squids[7].

[2] For example from 100 measurements, 50 will result in the excited, 50 in the unexcited state, leading to the conclusion that the qubit was in a 50/50 superposition. This deduction is made under the assumption that the qubit can be created in the same state over and over again, if the readout process changes the systems state.

where the angle θ can be seen as the mixture of $|\mathrm{H}\rangle$ and $|\mathrm{V}\rangle$, ϕ as the phase between them. Any vectors or matrices are written in the $|\mathrm{H}\rangle$, $|\mathrm{V}\rangle$ basis, if not stated otherwise. In vector representation they are chosen $|\mathrm{H}\rangle = \begin{pmatrix} 1 \\ 0 \end{pmatrix}$ and $|\mathrm{V}\rangle = \begin{pmatrix} 0 \\ 1 \end{pmatrix}$. Other polarization states can be expressed through these

$$\begin{aligned} |\mathrm{P}\rangle &= \frac{1}{\sqrt{2}}\left(|\mathrm{H}\rangle + |\mathrm{V}\rangle\right) \\ |\mathrm{M}\rangle &= \frac{1}{\sqrt{2}}\left(|\mathrm{H}\rangle - |\mathrm{V}\rangle\right) \\ |\mathrm{R}\rangle &= \frac{1}{\sqrt{2}}\left(|\mathrm{H}\rangle + i|\mathrm{V}\rangle\right) \\ |\mathrm{L}\rangle &= \frac{1}{\sqrt{2}}\left(|\mathrm{H}\rangle - i|\mathrm{V}\rangle\right) \end{aligned}$$

The convenient way to visualize a state of a single photon is through a vector on the *Bloch Sphere* (see figure 2.1) or *Poincaré Sphere* with the polarization states as the orthogonal axes. Originally this representation was developed by Henri Poincaré around 1892 to describe polarization states of light and adapted by Felix Bloch in 1964[1] to polarization states of 2 level systems. Effects of retarded (waveplates) and operations on the qubits are visible as paths of the state vector on the surface. This pictorial power makes the sphere a convenient tool of visualization.

Writing the polarization states as vectors, the *projection operator* of a state $|\psi\rangle$ is defined as $\mathcal{P} = |\psi\rangle\langle\psi|$. If this construct is acting onto another state $|a\rangle$

$$\mathcal{P}|a\rangle = |\psi\rangle\langle\psi|a\rangle$$

the projection of $|a\rangle$ onto $|\psi\rangle$ in the direction $|\psi\rangle$ is calculated, where $\langle\psi|a\rangle$ is the scalar product of the 2 vectors. This behaviour gives raise to the naming in analogy to 3d vectors. For example $|\mathrm{H}\rangle\langle\mathrm{H}|\psi\rangle$ corresponds to the projection of the green vector on $|\mathrm{H}\rangle$, that is its component along the positive z-direction. Two things are important to note:

- The above operation allows the extraction of components along e.g. an orthogonal base set and likewise to determine its base vectors in this set. However the state of the qubit is changed, so it is not possible to use "the same" again, moreover it has to be prepared in the same starting state again, or another one from the same source, in the same state must be used.
- In figure 2.1, $|\mathrm{H}\rangle$ is identified with the positive, $|\mathrm{V}\rangle$ with the negative z-direction. To anticipate chapter 2.2, a projection on either one of the previous vectors will be called "measuring along the z-direction". Likewise the other polarization types are identified with the generic x and y-direction.

Before turning to the full framework of measurements on qubits, the description of systems with more members reviewed.

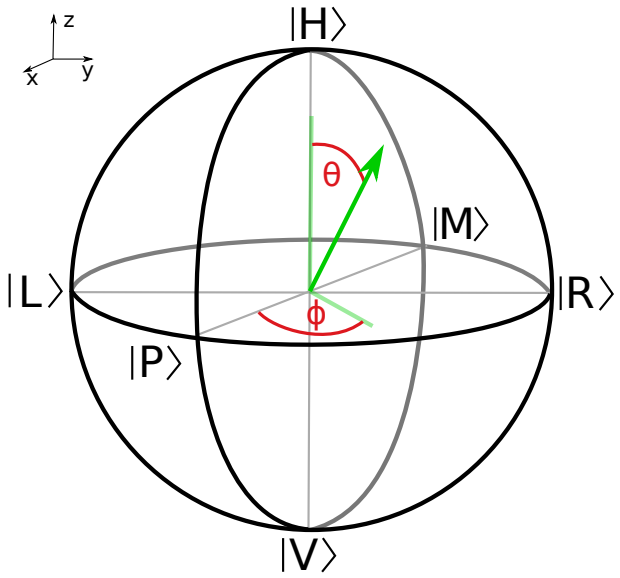

Figure 2.1: Representation of the base vector set $|H\rangle, |V\rangle$ $|P\rangle, |M\rangle$ and $|L\rangle, |R\rangle$ on the Poincaré or Bloch Sphere. Vectors in the x-y plane have no complex component. Vectors touching the surface of the sphere are identified as pure states, smaller ones as mixed states. By convention, the maximal length is 1. The lines in lighter green are projections onto the z-axis and x,y plane.

2.1.1 Multipartite states

To describe a system of more than one qubit, the above scheme has to be extended. Any vector that describes the state of a quantum system lives on a complex *Hilbert Space* $\mathcal{H}$ whose naming after David Hilbert originates from J. von Neumann who also introduced the bra and ket formalism of the state vectors[44]. If a system consist of multiple subsystems, then the Hilbert Space can be decomposed in subspaces of the corresponding systems.

$$\mathcal{H}_{1,2,3..N} = \mathcal{H}_1 \otimes \mathcal{H}_2 \otimes \mathcal{H}_3 \otimes \cdots \otimes \mathcal{H}_N$$

This gives the rules to calculate the vector representation for more than one member. For example

$$\begin{aligned} |\mathrm{H}\rangle_1 \otimes |\mathrm{V}\rangle_2 &= \begin{pmatrix} 1 \\ 0 \end{pmatrix} \otimes \begin{pmatrix} 0 \\ 1 \end{pmatrix} \\ &= \begin{pmatrix} 0 \\ 1 \\ 0 \\ 0 \end{pmatrix} \\ &= |\mathrm{HV}\rangle \end{aligned}$$

for a system of a horizontally and a vertically polarized photon. The last line is the commonly used shorthand notation where the order of the symbols mark the number of

the qubit so qubit 1 is said to be horizontally, qubit 2 vertically polarized. This space saving notation is kept during this work. Generally for 2 systems with the basis decomposition $|\psi\rangle = \sum_j a_j|e_j\rangle$ and $|\phi\rangle = \sum_k b_k|f_k\rangle$ any *product state* can be written

$$\begin{aligned} |\Psi\rangle &= \sum_j a_j|e_j\rangle \otimes \left(\sum_k b_k|f_k\rangle\right) \\ &= \sum_{j,k} c_{j,k}|e_j\rangle \otimes |f_k\rangle \end{aligned}$$

where the elements $c_{j,k} = a_j \cdot b_k$ form a tensor. Another way to see this value is as a vector with the dimension of subsystem 1 where each element is again a vector with dimension of subsystem 2. The above way of writing a quantum state is called *Schmidt Decomposition*, named after Erhard Schmidt. The number of $c_{j,k}$ is called the *Schmidt Rang*. Not all quantum states have high ranks as the above formula might suggest. A special group, named entangled states, has rang 1.

2.1.2 Entanglement

As soon as a qubit state is a superposition of different states, the claim that the Hilbert Space of a system can be decomposed in the subspaces of the subsystems does not hold any more. For example

$$|a\rangle = \frac{1}{\sqrt{2}}\left(|\mathrm{HV}\rangle + |\mathrm{VH}\rangle\right)$$

cannot be split in a state for each qubit. The 2 qubits are then called *entangled*[14]. The general definition reads[17]

> A pure state $|\psi\rangle$ is called a *product state* or *separable*, if there are 2 states $|\phi_A\rangle$ and $|\phi_B\rangle$ such that
>
> $$|\psi\rangle = |\phi_A\rangle \otimes |\phi_B\rangle$$
>
> If this is not the case, $|\psi\rangle$ is called *entangled*.

The above state is a version of the famous EPR-Bohm-source state, where an atom changing from the excited into the unexcited state emits 2 photons of orthogonal polarization in opposing directions. Measuring horizontal polarization in the first direction it is clear that the other photon must be vertically polarized or vice versa. The correlation between states is the essence of entanglement and cannot be described in mixtures.

2.1.3 Density matrices

The *density operator* or *density matrix* of a state $|\psi\rangle$is defined as $\rho = |\psi\rangle\langle\psi|$ and formally the projector onto this state. What is known as the density matrix formalism [44] can

describe mixture of different states. In quantum mechanics, the difference between superposition and mixture is crucial. Superpositions of states e.g. $|\mathrm{H}\rangle + |\mathrm{V}\rangle$ form again a state (in this case $|\mathrm{P}\rangle$) but a source can produce a certain number of $|\mathrm{H}\rangle$, $|\mathrm{V}\rangle$ and $|\mathrm{P}\rangle$ photons that must be described by their proper polarization. The state of the complete system is described as a (statistical) mixture of all contained states

$$\rho = \sum_i p_i |a_i\rangle\langle a_i|$$

with $\sum_i p_i = 1$. Given that only a single p_i is nonzero the state is said to be a *pure state* and $\rho^2 = \rho$ holds. In this case the expression reduces to the above projector on the only contained state.

This also illustrates that the density matrix describes a quantum mechanical state produced by a source or setup in total. Extracting this operator is equivalent to having full information on the state. However there are some requirements for the matrix to describe a *physical* state. For example calculations that lead to expected outcome probabilities of more than 100% are not considered physical and therefore the matrix leading to such results cannot describe a system that can possibly exist. Such effects are excluded if the matrix obeys:

Hermiticity: The density operator is a hermitian operator

$$\rho = \rho^\dagger$$

This means that the hermitian conjugate[3] or adjoint of the operator is again the operator

Proof: $(\rho)^\dagger = \left(\sum_i p_i |\psi_i\rangle\langle\psi_i|\right)^\dagger = \sum_i p_i \left(|\psi\rangle\langle\psi|\right)^\dagger = \sum_i p_i |\psi_i\rangle\langle\psi_i| = \rho$

Trace unity: The trace of any density operator is 1

$$\mathrm{Tr}\,(\rho) = 1$$

Proof: $\mathrm{Tr}\,(\rho) = \sum_{i,j} p_j \langle\psi_i|\psi_j\rangle\langle\psi_j|\psi_i\rangle = \sum_j p_j = 1$

This can be understood as normalization of probability. The diagonal elements of a density matrix represent the probability to measure the system in the state of the base vector of the corresponding row and column. The space of the complete operator is spanned by all base vectors, so the sum over the probabilities of all these must be unity.

[3] which is equivalent to transposing the matrix and taking the complex conjugate

Positivity: The operator ρ is a positive operator

$$\langle\psi|\rho|\psi\rangle \geq 0 \qquad \forall|\psi\rangle$$

Proof: $\langle\phi|\rho|\phi\rangle = \sum_i p_i\langle\phi|\psi_i\rangle\langle\psi_i|\phi\rangle = \sum_i p_i \left|\langle\phi|\psi_i\rangle\right|^2 \geq 0$

This is again a consequence of the probability interpretation. There are no negative probabilities.

2.1.3.1 Structure of a density matrix

Density operators of N qubit systems are 2^N times 2^N complex tensors. Values in the matrix depend on the basis vectors chosen. Standard bases are the bra end kets of horizontal and vertical polarization, in case of more than 1 member all permutations of them (see following example 2.1). They can be generated by counting in binary numbers from 0 to $2^N - 1$ and identifying $|\mathrm{H}\rangle$ with 0 and $|\mathrm{V}\rangle$ with 1[4]. In a 2 qubit example, the different rows and columns of the density matrix correspond to:

$$\rho = \begin{array}{c} \\ |\mathrm{HH}\rangle \\ |\mathrm{HV}\rangle \\ |\mathrm{VH}\rangle \\ |\mathrm{VV}\rangle \end{array} \begin{array}{c} \begin{array}{cccc} \langle\mathrm{HH}| & \langle\mathrm{HV}| & \langle\mathrm{VH}| & \langle\mathrm{VV}| \end{array} \\ \begin{pmatrix} \rho_{11} & \rho_{12} & \cdots & \\ \rho_{21} & \rho_{22} & & \\ \vdots & & \ddots & \\ \vdots & & & \end{pmatrix} \end{array} \tag{2.1}$$

Entries on the diagonal reflect the probability for the system to be in the state of the row, respectively the column base vector. For $|\mathrm{HH}\rangle$ this would be $\rho_{11} = \langle\mathrm{HH}|\rho|\mathrm{HH}\rangle$. Off-diagonal elements show correlations between those state. For example an entry in the first row and last column, $\langle\mathrm{HH}|\rho|\mathrm{VV}\rangle$, shows that $|\mathrm{HH}\rangle$ and $|\mathrm{VV}\rangle$ are present in a certain ratio. An example would be the the state $|\psi\rangle = \frac{1}{\sqrt{2}}(|\mathrm{HH}\rangle + |\mathrm{VV}\rangle)$. The density operator is calculated as

$$\begin{aligned} |\psi\rangle = \frac{1}{\sqrt{2}}\left(|\mathrm{H}\rangle\otimes|\mathrm{H}\rangle + |\mathrm{V}\rangle\otimes|\mathrm{V}\rangle\right) &= \frac{1}{\sqrt{2}}\left[\begin{pmatrix}1\\0\\0\\0\end{pmatrix} + \begin{pmatrix}0\\0\\0\\1\end{pmatrix}\right] = \frac{1}{\sqrt{2}}\begin{pmatrix}1\\0\\0\\1\end{pmatrix} \\ \Downarrow & \\ \rho = |\psi\rangle\langle\psi| &= \frac{1}{2}\begin{pmatrix}1&0&0&1\\0&0&0&0\\0&0&0&0\\1&0&0&1\end{pmatrix} \end{aligned}$$

[4] For example 42 corresponds to 101010 which gives $|\mathrm{HVHVHV}\rangle$

Elements show that with equal probability either $|\mathrm{HH}\rangle$ or $|\mathrm{VV}\rangle$ will be measured and the state to be a superposition. A mixture of the same states would lead to $\rho = \frac{1}{2}\begin{pmatrix} 1 & 0 & 0 & 0 \\ 0 & 0 & 0 & 0 \\ 0 & 0 & 0 & 0 \\ 0 & 0 & 0 & 1 \end{pmatrix}$ missing the off-diagonal elements.

2.1.3.2 Entanglement between systems

Not only single qubits but complete systems can be entangled, so the definition for entanglement can be extended to density operators[45].

> A state described by ρ is a *product state*, if two states ρ_A and ρ_B exist, such that
>
> $$\rho = \rho_A \otimes \rho_B$$
>
> The state is separable if
>
> $$\rho = \sum_i p_i \left(\rho_A\right)_i \otimes \left(\rho_B\right)_i$$
>
> with complex parameters p_i. Otherwise the state is *entangled*.

It might seem that entanglement is solely of academic interest, because most experiments use well isolated systems. There are experiments that demonstrate entanglement in macroscopic systems[23] but the effect is small and short-lived. However it can be used to push the so called "classical limits". An example would be the Rayleigh diffraction limit[4] which states that a structures smaller than half the illuminating wavelength, cannot be resolved and likewise exposed to light. Entangled photons allow the engineering of even smaller structures[5] or increased accuracy in interferometers[27].

2.1.4 Measures

Having reconstructed a density matrix from measurements, one could ask how good the state was prepared in comparison to the expected version or if it is a pure state. There are several measures for this

Purity Gives a measure if the density operator describes a pure state or a mixed one.

$$P\left(\rho\right) = \mathrm{Tr}\left(\rho \cdot \rho\right)$$

> By definition of the idempotency of pure states and the constraint of trace unity it is clear that a pure state will have trace 1. A complete mixture will result in a value of $\frac{1}{d}$ where d are dimensions of ρ. Calculating the purity will show whether a mixture has been observed or not.

Fidelity Is a distance measure between 2 states and commonly used to characterizes the quality of a produced state. For this the measured state is compared to the expected one. The fidelity between 2 states ρ and ϕ is calculated as

$$F(\rho, \phi) = \mathrm{Tr}\left(\sqrt{\sqrt{\rho}\phi\sqrt{\rho}}\right)$$

and is part of the Bures Distance[8] that is the finite version of the original Bures metric. Because $\rho^2 = \rho$ holds for pure states , the expression reduces to

$$F(\rho, \phi) = \mathrm{Tr}(\rho\,\phi) = \langle\phi|\rho|\phi\rangle$$

which is the expectation value of one state with respect to the other. Accordingly the fidelity is 1 if the density operators describe the same state. This is the standard tool when density matrices, recovered from data are compared to expected states.

Another distance measure is the

Trace distance also called the *Kolmogorov Distance* or *trace norm distance*[16]

$$\delta(\rho, \phi) = \frac{1}{2}\mathrm{Tr}(\rho - \phi)$$

The original distance measure was developed for probability distributions in general, but as density operators describe the probability distribution for a state, the expression can be cast into this form for such operators.

There exist a lot more types of measures but for a general inspection of the results, the above suffice.

2.2 Measurements

In quantum mechanics, observables are represented by hermitian operators. A state being in a superposition $|\psi\rangle = \sum_i c_i|a_i\rangle$ will be forced into an eigenstate (any $|a_k\rangle$) of the operator when the corresponding observable is measured. This is also why measurements are often called projective measurements, as they project the original state onto another one.

$$\rho_a|\psi\rangle = |a\rangle\langle a|\psi\rangle = c|a\rangle$$

where $c = \langle a|\psi\rangle$ is the projection of $|\psi\rangle$ along $|a\rangle$.

The expectation value of an observable O with respect to a state $|a\rangle$ is defined as

$$\begin{aligned}\langle a|O|a\rangle &= \sum_i \langle a|i\rangle\langle i|O|a\rangle \\ &= \sum_i \langle i|O|a\rangle\langle a|i\rangle \\ &= \sum_i \langle i|O\,\rho_a|i\rangle \\ &= \mathrm{Tr}(O\,\rho_a) \end{aligned} \tag{2.2}$$

This expression already occurred in the definition of the fidelity for pure states.

For photonic qubits a generic observable reads

$$O(\theta,\phi) = \cos(\theta)\,\sigma_z + \cos(\phi)\sin(\theta)\,\sigma_x + \sin(\phi)\cos(\theta)\,\sigma_y \tag{2.3}$$

where the angles θ and ϕ identify an axis through the origin of the Bloch Sphere. The Pauli Spin Matrices[5]

$$\sigma_x = \begin{pmatrix} 1 & 0 \\ 0 & -1 \end{pmatrix} \qquad \sigma_y = \begin{pmatrix} 0 & -i \\ i & 0 \end{pmatrix} \qquad \sigma_z = \begin{pmatrix} 0 & 1 \\ 1 & 0 \end{pmatrix}$$

form the orthogonal basis set that spans the space. The polarization states of the photonic qubit can be identified with the eigenstates of the Pauli Matrices

$$\begin{aligned} \sigma_x|\mathrm{P/M}\rangle &= \pm|\mathrm{P/M}\rangle \\ \sigma_y|\mathrm{R/L}\rangle &= \pm|\mathrm{R/L}\rangle \\ \sigma_z|\mathrm{H/V}\rangle &= \pm|\mathrm{H/V}\rangle \end{aligned}$$

This justifies the previous geometric interpretation of an axis through the sphere and identifies $\sigma_{x,y,z}$ as the 3 generic and orthogonal directions x,y and z. Measuring the expectation value of, for instance σ_y, is equivalent to project the state onto the y-axis and the process will just be called "measuring along the y-axis".

In an experiment, one does not aim to project along an axis but merely on a specific state. A handy expression for the projector on a polarization state in terms of its Pauli Matrix is[6]

$$\mathcal{P}_{i,\pm} = \frac{1}{2}(1 \pm \sigma_i) \tag{2.4}$$

where the sign is equal to the one of the eigenvalue one wants to project onto. This expression is only valid for systems of 2 members and used to calculate the probability to measure the qubit in a certain polarization state via $\mathrm{Tr}(\mathcal{P}_{i,\pm}\rho)$.

Observables for systems with more than one qubit, can be calculated in a similar way using the tensor product. Acting only on qubit 1 in a 2 qubit system, the operator of the observable is written as $O_1 \otimes \mathbb{1}$ or likewise $\mathbb{1} \otimes O_2$ for qubit 2. The combined operator reads $O_1 \otimes O_2$. Also effects of wave plates are described by operators (see chapter 2.3 for expressions), consecutive operations by products of the operators. Combined with tensor products, operators act only on their subspace and so do successive operations

$$(A_1 \otimes A_2)\cdot(B_1 \otimes B_2) = (A_1 \cdot B_1) \otimes (A_2 \cdot B_2)$$

[5]There is a fourth Pauli Matrix, the unit matrix $\sigma_0 = \begin{pmatrix} 1 & 0 \\ 0 & 1 \end{pmatrix}$ that is left out here, but is needed int he following formulas to reconstruct the density matrix. Often instead of $\{x,y,z\}$ the labels $\{1,2,3\}$ are used

[6]Any pauli matrix can be decomposed as $\sigma_i = |+\rangle\langle+| - |-\rangle\langle-|$ with $|+\rangle$ the positive eigenvector and $|-\rangle$ the negative eigenvector. Also $\mathbb{1} = |+\rangle\langle+| + |-\rangle\langle-|$ and therefore $\mathbb{1} = |+\rangle\langle+| + |+\rangle\langle+| - \sigma_i = 2|+\rangle\langle+| - \sigma_i$ $\rightarrow |+\rangle\langle+| = \frac{1}{2}(\mathbb{1} + \sigma_i)$ and analogue for $|-\rangle\langle-|$

In general, multiplication of operators is not commutative, but associative

$$A\,(B\cdot C) = (A\cdot B)\,C \neq (B\cdot A)\,C$$

Their commutation behaviour is described by the *commutator*, defined as $[A,B] = AB - BA$. If it is zero, they commute, otherwise they commute as stated. For example the pauli matrices obey

$$[\sigma_i, \sigma_j] = 2\,i\,\varepsilon_{ijk}\sigma_k$$

with the Levi-Civita symbol ε_{ijk}. This would lead to $\sigma_x\sigma_y = \sigma_y\sigma_x - 2i\sigma_z$.

This relation reflects the surprising fact that certain measurements in quantum mechanics are order sensitive. The outcome will change depending on the order they are performed, something not known from macroscopic systems. The previous section shows that this is a result of the state being projected onto an eigenstate of the observable and therefore being subject to change.

2.3 Measuring photonic qubits

To analyze the polarization of a photonic qubit, a polarizing beam splitter (PBS), a quarter wave plate (QWP or $\frac{\lambda}{4}$-plate), a half wave plate (HWP or $\frac{\lambda}{2}$-plate) and a single photon counting module (here Avalanche Photo Diodes) are arranged to a *polarization analysis block* (fig. 2.2b).

The PBS will split an unpolarized light beam into its horizontal and vertical component (see figure 2.2a) or likewise distribute photons according to their projection onto the $|\mathrm{H}\rangle$,$|\mathrm{V}\rangle$ (or z) axis (base). For example P polarized photons will be detected with equal probability in either the horizontal or vertical output channels. H polarized ones on the other side with 100% (for an ideal PBS) in the horizontal one. Because the probability depends on the projection onto the z base, a PBS will experimentally implement the operation $\mathrm{Tr}\,(\sigma_z\rho)$. If one is interested in the probabilities for a detection in either output channel, one has to calculate $\mathrm{Tr}\,(\mathcal{P}_{z,+}\rho)$ for $|\mathrm{H}\rangle$ or $\mathrm{Tr}\,(\mathcal{P}_{z,-}\rho)$ for $|\mathrm{V}\rangle$. Detection in the APD absorbs the photon, so the source used needs to produce the same state with high reliability because consecutive measurements are necessary to collect enough data. To realize arbitrary measurement directions (see eq. 2.3), the combination of a HWP, QWP and a PBS is necessary.

A HWP rotates the state vector by 180° around an axis in the $|\mathrm{H}\rangle|\mathrm{V}\rangle$-$|\mathrm{P}\rangle|\mathrm{M}\rangle$ plane, given by 2 times the physical rotation (α) (in the plane perpendicular to the incident beam) of the crystal itself. The 0° position is defined as the position where horizontal polarized light stays horizontal and vertical polarized stays vertical or in other words the rotation axis concurs with the z-axis in the Bloch Sphere. The operator for a HWP reads

$$\begin{aligned}\mathrm{HWP}\,(\alpha) &= \begin{pmatrix} \cos(2\alpha) & \sin(2\alpha) \\ \sin(2\alpha) & -\cos(2\alpha) \end{pmatrix} \\ &= \sin(2\alpha)\,\hat{\sigma}_x + \cos(2\alpha)\,\hat{\sigma}_z \end{aligned} \tag{2.5}$$

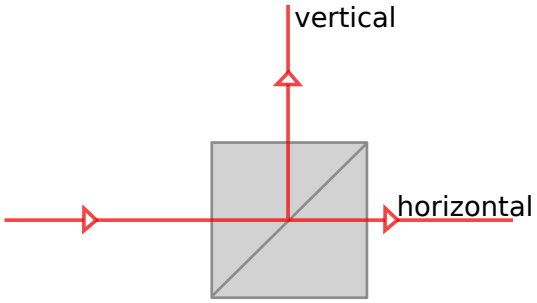

(a) Scheme of a PBS. Horizontal polarized light will be transmitted, vertical polarized light will be reflected

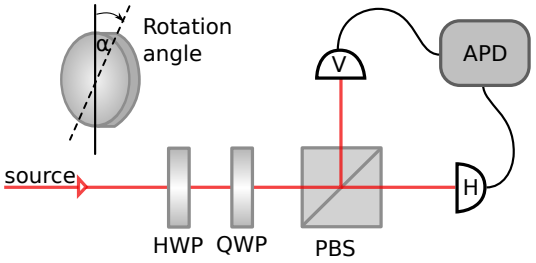

(b) Scheme for measuring in an arbitrary base. The beam passes through a quarter wave plate (QWP), a half wave plate (HWP) and the polarizing beam splitter (PBS). Each output channel of the PBS is then fed into one avalanche photo diode (APD). Different measurement bases are created for different rotation angles α of the wave plate.

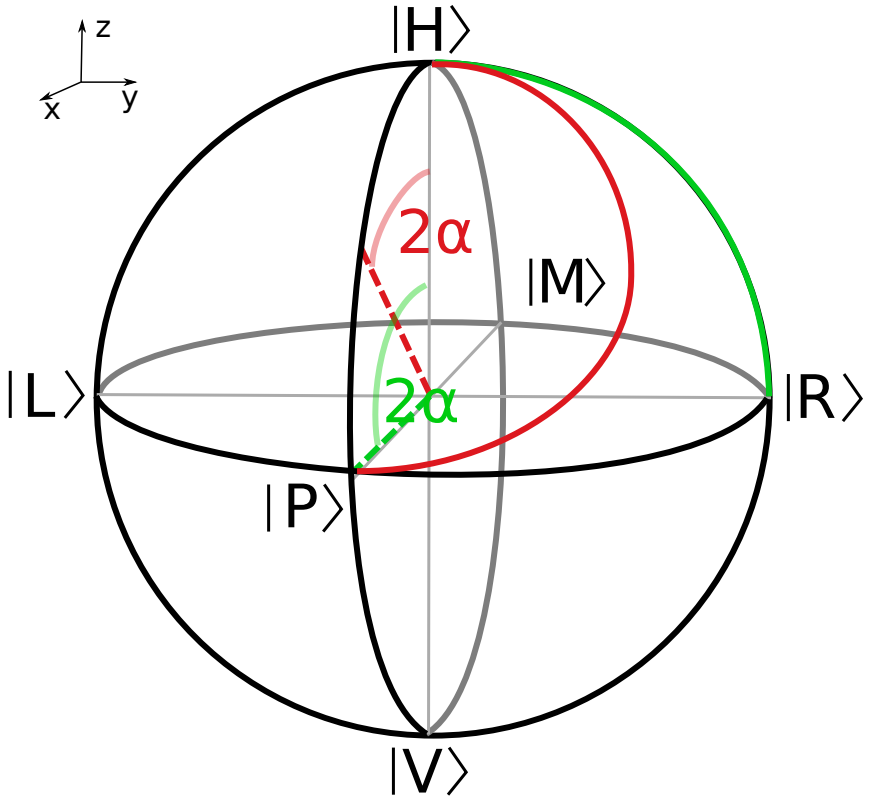

(c) Effect of a QWP, green (HWP, red) onto $|H\rangle$ polarized light. The Bloch vector is rotated by 90° (180°) around the dotted line in the $|H\rangle$-$|P\rangle$ plane. In the order of figure 2.2b any measurement direction can be reached. The angle α is the physical rotation of the corresponding wave plate (shown in the corresponding color).

Figure 2.2: Tools to measure polarization of photons and their effect on polarization.

The effect on a vertically polarized photon propagating through a HWP rotated by 45° is that it will become horizontally polarized or likewise plus polarized when incident on a 22.5° rotated HWP (red line in figure 2.2c).

A QWP rotates the state vector by 45° around an axis with the same definition as in the HWPs' case. The operator reads

$$\begin{aligned} \mathrm{QWP}(\alpha) &= \begin{pmatrix} \cos^2(\alpha) - i\sin^2(\alpha) & (1+i)\cos(\alpha)\sin(\alpha) \\ (1+i)\cos(\alpha)\sin(\alpha) & -i\cos^2(\alpha) + \sin^2(\alpha) \end{pmatrix} \\ &= \frac{1}{2}\left[(1-i)\,1 + 2\,(1-i)\cos(\alpha)\sin(\alpha)\,\hat{\sigma}_x + (1+i)\cos(2\alpha)\,\hat{\sigma}_z\right] \end{aligned} \tag{2.6}$$

and will rotate a right polarized photon into horizontal polarization for a wave plate rotation of 45° (green line in figure 2.2c).

When measuring in arbitrary bases, the idea is to rotate the positive eigenvector ($|\mathrm{R}\rangle$ or $|+\rangle$) onto $|\mathrm{H}\rangle$ and the negative one ($|\mathrm{L}\rangle$ or $|-\rangle$) onto $|\mathrm{V}\rangle$. This way, the PBS will effectively project onto the positive or negative eigenvector of the desired direction. The angles of the wave plates for the 3 standard directions are

measurement direction	HWP	QWP
X (σ_x)	22.5°	0°
Y (σ_y)	0°	45°
Z (σ_z)	0°	0°

To measure along an arbitrary direction, the relation

$$\hat{\sigma}_z = [\mathrm{QWP}(\alpha_2) \cdot \mathrm{HWP}(\alpha_1)]\,\hat{\sigma}(\theta,\phi)\,[\mathrm{QWP}(\alpha_2)\,\mathrm{HWP}(\alpha_1)]^\dagger \tag{2.7}$$

has to be solved. The solutions are ambiguous but will result in the correct outgoing polarization.

A complete setup for the analysis of a single photonic qubit state is shown in figure 2.2b. This scheme is however not the only possible one. Another implementation would exchange the PBS by a polarizer[22]. Downside of this approach is the loss in count rate, because photons that are projected onto the orthogonal state for which the polarizer is transmittive, are lost. In the later chapters it will become clear that high count rates are crucial, thus the version with a PBS is chosen.

3 Quantum State Tomography

Tomography originates from the Greek word "tomos" that means "part" and "graphein" what can be translated as "to write". From a set of images that contain reduced information about the object, the complete object is reconstructed. For example the 3D content of a picture can be extracted from several 2D pictures taken from different directions. This is also the basic idea for quantum state tomography where the state is projected on a set of different bases, called the *tomographic set*. Instead of extracting just a single property via so called witnesses e.g. entanglement[17], state tomography aims to extract all possible information about the state that are contained in the density operator. Section 2.1.3 motivated the structure of the density matrix and showed that knowledge of this operator suffices to describe a system in total. Behaviour under certain operations and measurement outcomes can be calculated. This means that from the measurement of selected properties of a system, other can be inferred and this is what tomography is about. In the following sections, state tomography of single qubits will be introduced and later on extended arbitrary qubit numbers. Because the amount of data that need to be measured scales exponentially in the number of qubits, a different and more effective but more restrictive tomography method is presented. In this new scheme the data increase can be reduced to a quadratic scaling of the qubit number.

3.1 Tomography of a single qubit

The state of a qubit, represented by a vector in the Bloch Sphere, is fixed by 3 parameters. Either 2 angles and the length of the vector, like in spherical coordinates, or 3 values that are the projections on a set of 3 orthogonal axes, like the standard x,y and z-axis convention. Previously it was shown that measuring the expectation values of σ_x, σ_y and σ_z is the equivalent to a projection on the generic x,y and z directions.

Descriptions of polarized light have a longer history than states of qubits and were developed for light beams rather than individual photons. Nevertheless, the same scheme can be used for qubits. The commonly used parameters were introduced by G. G. Stokes in 1852 and are therefore called the *Stokes Parameter*. They are defined in terms of electric field amplitudes for different types of polarization[4] and originally motivated the

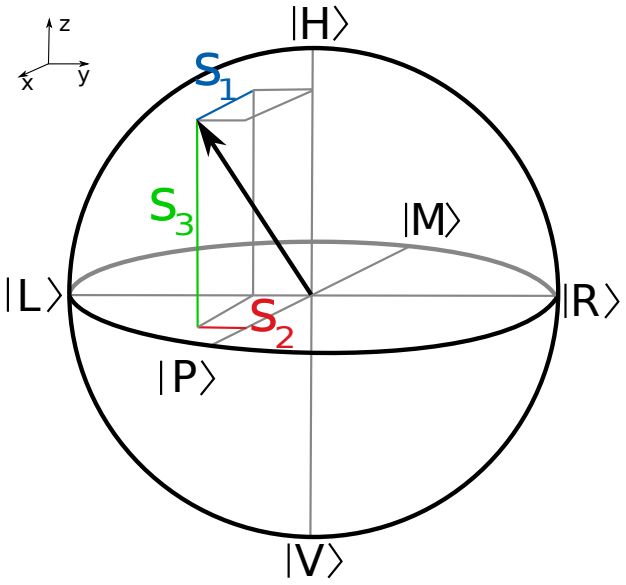

Figure 3.1: Stokes parameters in the Bloch Sphere

visualization on a sphere. They are defined as:

$$\begin{aligned} S_0 &= |E_H|^2 + |E_V|^2 \\ S_1 &= |E_P|^2 - |E_M|^2 \\ S_2 &= |E_R|^2 - |E_L|^2 \\ S_3 &= |E_H|^2 - |E_V|^2 \end{aligned}$$

Here $|E_H|^2$ is the amplitude of the horizontally polarized field; other possible polarizations are plus (P) and minus (M), left (L) and right (R). The first one, S_0, can be understood as the intensity of the beam and has therefore no analogon in the bloch sphere. S_1 to S_3 represent the "amount" of H/V, L/R or P/M polarization.

Single photons are recorded as clicks in the detectors in either the horizontal or vertical channel after the PBS. The Stokes Parameters can be rewritten into a more appropriate form

$$\begin{aligned} S_0 &= P_{|H\rangle} + P_{|V\rangle} \\ S_1 &= P_{|P\rangle} - P_{|M\rangle} \\ S_2 &= P_{|R\rangle} - P_{|L\rangle} \\ S_3 &= P_{|H\rangle} - P_{|V\rangle} \end{aligned}$$

where $P_{|a\rangle}$ stands for the probability to detect a photon in state $|a\rangle$. S_1 to S_3 are normalized by S_0 that they can vary between -1 and +1. This way, their values match the signs of the eigenvalues of the σ matrices, that were identified with the axes earlier. For example $S_3 = +1$ corresponds to $|\mathrm{H}\rangle$ or $S_2 = -1$ to . Recorded number of events can be transformed

to a value reflecting the probability by normalizing with the total number of events during the measurement.

$$P_{|a\rangle} \approx \frac{N\left(|a\rangle\right)}{N_{\text{total}}} \tag{3.1}$$

The $\approx$ is used here, because equality only holds for $N \to \infty$. Otherwise the calculated value is somewhere near the probability and should better be interpreted as a frequency[3]. Especially for low count rates the adequate usage of the above relation should be kept in mind. Such considerations are mostly important for correct error estimation and if the reconstructed density matrix is to be used in further calculations. General features like the structure, are visible without notice.

In figure 3.1 the Stokes Parameters are visualized for a qubit state. Because of the reassembly with the classical x,y and z directions, the numerical subindices are often dropped and replaced by the axis labels. Having measured their values, the density matrix can be calculated via[31]

$$\rho = \frac{1}{2}\sum_{i=0}^{3}\frac{S_i}{S_0}\,\sigma_i$$

Although the orthogonal axes represented by the Pauli Matrices are chosen, another, not necessarily orthogonal, set can be used as well. However, uncertainties will increase.

3.2 Multiqubit Tomography

To use the above idea for more than one qubit, each one has to be accessible locally, which means its measurement is independent of the remaining system and also leaves the remaining system untouched. The exact prerequisites to the setup will be explained later in the experimental part. A generalization of the Stokes Parameters to N qubits yields[31]

$$\rho = \frac{1}{2^N}\sum_{i_1,i_2,\ldots i_N=0}^{3} T_{i_1,i_2,\ldots i_N}\sigma_{i_1}\otimes\sigma_{i_2}\otimes\cdots\sigma_{i_N} \tag{3.2}$$

The first, numerical value before the sum, is just a normalization constant for N qubits. The tensor (T) contains the (measured) values that are identified with a certain base combination[1] and will be explained after the next paragraph. The tensor product of pauli matrices reflects the choice of basis. Again, only orthogonal measurement direction (x,y or z) are chosen. In a 2 qubit example with projection directions as axis labels instead of i_n, one term could read

$$\sigma_x\otimes\sigma_z \;\; = \;\; \left(\sigma_x\otimes\mathbb{1}\right)\left(\mathbb{1}\otimes\sigma_z\right)$$

which corresponds to a measurement along the x-axis on qubit 1 and z-axis on qubit 4. The according T entry has the label T_{XZ}, so the measurement directions are coded in the

[1] Bases are coded as $i = 0 \Rightarrow \sigma_0 = \mathbb{1}$; $\sigma_1 = \sigma_x$, $\sigma_2 = \sigma_y$ and $\sigma_3 = \sigma_z$

order and label of the subindex. When for a single qubit the orthogonal bases, including the (normalized) intensity parameter, had to be measured, for multiple qubits all combinations for all members are needed. For example the element T_{X1} with the corresponding operator $\sigma_x \otimes \mathbb{1}$ or T_{1Y} with $\mathbb{1} \otimes \sigma_y$. Normalization is done with respect to $T_{11\ldots1} \stackrel{!}{=} 1$, so there are in general $2^N \times 2^N - 1$ entries that have to be determined through measurements.

The use of the PBS allows a so called *overcomplete measurement*. For this, it is instructive to have a look at the T entries and how they relate to the one qubit Stokes Parameters. In a small 2 qubit example, one could naively write

$$\begin{aligned} T_{ZY} &= T_Z \otimes T_Y \\ &= S_3 \otimes S_2 \\ &= \left(P_{|H\rangle} - P_{|V\rangle}\right) \otimes \left(P_{|R\rangle} - P_{|L\rangle}\right) \\ &= P_{|HR\rangle} - P_{|HL\rangle} - P_{|VR\rangle} + P_{|VL\rangle} \end{aligned} \tag{3.3}$$

where the tensor product is used here to discriminate between measurements on qubit 1 and qubit 2 and should not be regarded as a mathematical operation. The last line shows that the needed values are for example the probability to measure qubit 1 in state $|H\rangle$ and simultaneously qubit 2 in state $|R\rangle$ ($P_{|HR\rangle}$) and the other permutations for the used bases. If a "$\mathbb{1}$ measurement" is involved, the expression reads

$$\begin{aligned} T_{1Y} &= T_1 \otimes T_Y \\ &= S_0 \otimes S_2 \\ &= \left(P_{|H\rangle} + P_{|V\rangle}\right) \otimes \left(P_{|R\rangle} - P_{|L\rangle}\right) \\ &= P_{|HR\rangle} - P_{|HL\rangle} + P_{|VR\rangle} - P_{|VL\rangle} \end{aligned} \tag{3.4}$$

so the same values as for the previous expression can be used. To make use of the PBS, events in all channels have not only to be recorded, but also concurrent events. The analysis of a single qubit requires the measurement of H and V events. Already for 2 qubits, simultaneous events in channel H on qubit 1 and channel V on qubit 2 (and all other permutations) are possible. Although one settings (like T_{ZX} or T_{1Y}) is said to be one measurement, 2^N values are recorded: the concurrent detections of photons in different PBS output configurations (like HH, HV, VH and VV). A scheme of a 2 qubit example is shown in figure 5.3, illustrating possible combinations. Because a large number of recorded values is reduced to fewer T entries, this scheme is called *overcomplete*.

One benefit is that tensor entries including a 1, can be calculated by averaging over measurements in an arbitrary base on the qubit where the "1 measurement" needs to be performed. In eq. 3.4 the pair H/V was used for S_0, but this choice is arbitrary. H/V, R/L or P/M are equally suited. A 2 qubit T tensor has the structure

T_{11}	T_{1X}	T_{1Y}	T_{1Z}
T_{X1}	T_{XX}	T_{XY}	T_{XZ}
T_{Y1}	T_{YX}	T_{YY}	T_{YZ}
T_{Z1}	T_{ZX}	T_{ZY}	T_{ZZ}

with the $T_{11} = 1$ normalized entry marked in dark gray and the ones that are calculated from values in the corresponding row or column in lighter gray. Instead of $2^N \times 2^N - 1 = 4^N - 1$, only $3^N - 1$ unique settings (combinations of measurement bases) need to be determined, if correlations in the outputs of the PBS are recorded.

There are no restrictions to the state analyzed via this scheme, so it is called *Full Tomography*. A major problem of multiqubit states produced by most sources and is the low count rate, if one seeks states with large numbers of genuine entangled qubits. Because correlation information are important to detect entanglement, the number of terms in the standard tomography scheme increases exponentially in the number of qubits $(3^N - 1)$. For reasonable statistics, time needed for the measurement increases with the same rate. This combination of exponential increase in time and exponential decrease in brightness immediately leads to problems. For the described experiment, the analysis of the 6 qubit symmetric Dicke State, full tomography is already out of reach. Good statistics would require a month of 24h a day, 7 days a week non-stop measurement, what is not possible with the used setup. Using symmetries in the states allows a reduction to 24h of measurement time with the same precision. The vast difference in the necessary time reflects the reduction of individual measurement settings from $\mathcal{O}\left(3^N\right)$ to $\mathcal{O}\left(N^2\right)$.

3.3 Permutationally Invariant Quantum State Tomography

Most states of interest show certain symmetries. They can be chosen on purpose, because the state is more tolerant against loss of entanglement if individual photons are lost, or the process in the source impresses its symmetry. The following is designed for *permutationally invariant* (PI) states. Such states are invariant under exchange of arbitrary qubits. A simple example would be the bell state $\frac{1}{\sqrt{2}}\left(|\mathrm{HV}\rangle + |\mathrm{VH}\rangle\right)$; summation ensures that exchange of qubit 1 and 2 will just change the order, with no effect for the overall state. $|\Psi^-\rangle = \frac{1}{\sqrt{2}}\left(|\mathrm{HV}\rangle - |\mathrm{VH}\rangle\right)$ on the other hand does not obey this symmetry because the phase factors in front of the polarization states are not recovered.

The formal definition of PI symmetry is[40]

$$\rho_{\mathrm{PI}} = \frac{1}{N!}\sum_k \Pi_k \rho \Pi_k$$

where Π_k are the permutations of all qubits. Any density operator has a part that fulfills the above equation, but the state it describes does not necessarily lie in this subspace. With this in mind, one can state that any density operator has a part that is permutationally invariant, and a part that is not:

$$\rho = \rho_{\mathrm{nonPI}} + \rho_{\mathrm{PI}}$$

The downside of PI tomography is, that the ρ_{nonPI} part will not be visible. Fortunately white noise, which is of most interest when characterizing an experiment in terms of performance, is PI symmetric and will therefore be visible.

Permutational Invariant Quantum State Tomography is covered in full detail in[40], the most important points will be highlighted in the following. Any symmetry of the state must be mapped to the values recorded in a full tomography approach. If the state is invariant under exchange of qubits, then this will be true for measurements in base configurations that differ in the exchange of qubits as well. For instance it does not matter if qubit 1 is measured along the x-basis and qubit 2 along the y-basis, or the other way round. So assumingly a projector of the form $\sigma_x \otimes \sigma_y$ would have the same measurement result as $\sigma_y \otimes \sigma_x$. The T tensor from the previous example will become symmetric on the diagonal:

T_{11}	T_{1X}	T_{1Y}	T_{1Z}
T_{X1}	T_{XX}	T_{XY}	T_{XZ}
T_{Y1}	T_{YX}	T_{YY}	T_{YZ}
T_{Z1}	T_{ZX}	T_{ZY}	T_{ZZ}

Same colour indicates identical numerical values. A consequence is, that the order in the base configuration is not important, but the amount of qubits that are measured in a certain basis. For example the values of $T_{XXY} = T_{XYX} = T_{YXX}$ should be equal. A short hand notation would be

$$T_{XXY} = T_{XYX} = T_{YXX} \Leftrightarrow \langle X^{\otimes 2} \otimes Y^{\otimes 1} \otimes Z^{\otimes 0} \otimes \mathbb{1}^{\otimes 0} \rangle$$

X stands for measurements in σ_x, Y in σ_y and Z in σ_z. For N qubits the generic expression is

$$\langle X^{\otimes k} \otimes Y^{\otimes l} \otimes Z^{\otimes m} \otimes \mathbb{1}^{\otimes n} \rangle \tag{3.5}$$

with $k+l+m+n = N$. Instead of measuring locally in different bases, all qubits are locally projected onto the same axis in the Bloch Sphere[2] and therefore measured in the same basis. A local basis $\{|\phi_1\rangle, |\phi_2\rangle\}$ corresponds to an measurement operator $A = |\phi_1\rangle\langle\phi_1| - |\phi_2\rangle\langle\phi_2|$ if ϕ_1 is the eigenvector with the positive eigenvalue and ϕ_2 the one with the negative. Not only $\langle \left(A^{\otimes N}\right)_{\mathrm{PI}} \rangle$ is determined, but simultaneously all

$$\langle \left(A^{\otimes (N-n)} \otimes \mathbb{1}^{\otimes n}\right)_{\mathrm{PI}} \rangle \tag{3.6}$$

with $n = 0, ..., N-1$[3] because PBS are used and the same calculation trick as before can be utilized. The subscript $_{\mathrm{PI}}$ marks the setting as sensitive only to the PI part of the state. To find the number of needed settings is to find the relation to the standard bases (x,y and z) to the A. The terms like 3.6 can be related to the standard bases via

$$\langle \left(X^{\otimes k} \otimes Y^{\otimes l} \otimes Z^{\otimes m} \otimes \mathbb{1}^{\otimes n}\right)_{PI} \rangle = \sum_{j=1}^{\mathcal{D}_N} c_j^{(k,l,m)} \langle \left(A_j^{\otimes (N-n)} \otimes \mathbb{1}^{\otimes n}\right)_{PI} \rangle \tag{3.7}$$

[2]It is possible to measure different settings on each qubit, but then the number of overall measurements will not be minimal!

[3]$A^{\otimes n} = \bigotimes_n A = \underbrace{A \otimes A \otimes \cdots A}_{n \text{ times}}$

$\mathcal{D}_N$ then is the number of settings that are needed to calculate ρ, with a small detour over the 3.5 terms. Its value is found by some combinatorial considerations, finding the space spanned by 3.5.

The most exact information about a vector is given in terms of an orthogonal base set. If projective measurements of a qubit are just performed onto the H/V,P/M plane, there is no chance to determine a state correctly that has contributions in the R/L direction. Merely its projection onto the plane is measured. The result space then can be considered to be of lower dimension than the source space. To determine $\mathcal{D}_N$, the dimension of the space spanned by 3.5 needs to be found[4], because eq. 3.7 states that the same space is spanned by $\mathcal{D}_N$ directions of type 3.6.

Overall there are

$$\mathcal{D}_{N-n} = \begin{pmatrix} N-n+2 \\ N-n \end{pmatrix}$$

possibilities where $k+l+m+n=N$ holds and a previously unknown direction is covered. In other word the term describes the expectation value of a measurement direction that is orthogonal to all previous ones. All terms of type 3.5 contribute one expectation value, because the state can be projected along each counted dimension. For $n > 0$ $\mathcal{D}_{N-n}$ decreases, so to map the full tomographic set to the new directions A_j, $\mathcal{D}_N$ settings must be chosen. Otherwise less dimensions could be covered and not the full state but the projection on a subspace is measured. The necessary number can then be calculated via

$$\mathcal{D}_N = \begin{pmatrix} N+2 \\ N \end{pmatrix} = \frac{1}{2}\left(N^2+3N+2\right) \tag{3.8}$$

From the afore shown decomposition the values of T for eq. 3.2 can be calculated. What is left now is to find a set of A_j and c_j. The overall statistical uncertainty needs to be minimized, which is the sum of the variances of the Bloch vector

$$\left(\mathcal{E}_{\text{total}}\right)^2 = \sum_{k+l+m+n=N} \mathcal{E}^2\left[\left(X^{\otimes k}\otimes Y^{\otimes l}\otimes Z^{\otimes m}\otimes \mathbb{1}^{\otimes n}\right)\right]\frac{N!}{k!l!m!n!}$$

where the variance of a single element is

$$\mathcal{E}^2\left[\left(X^{\otimes k}\otimes Y^{\otimes l}\otimes Z^{\otimes m}\otimes \mathbb{1}^{\otimes n}\right)\right] = \sum_{j=1}^{\mathcal{D}_N}\left|c_j^{(k,l,m)}\right|^2 \underbrace{\mathcal{E}^2\left[\left(A_j^{\otimes(N-n)}\otimes \mathbb{1}^{\otimes n}\right)_{\text{PI}}\right]}_{*}$$

The variance of expression * depends on the statistic of the experiment. For the following photonic setup, a Poissonian distribution can be assumed

$$\mathcal{E}^2\left[\left(A_j^{\otimes(N-n)}\otimes \mathbb{1}^{\otimes n}\right)_{\text{PI}}\right] = \frac{\left[\Delta\left(A_j^{\otimes(N-n)}\otimes \mathbb{1}^{\otimes N}\right)_{\text{PI}}\right]^2_{\rho_0}}{\lambda_j - 1}$$

[4]This is valid because these terms are known from full tomography to span the full result space

with the Poisson Parameter λ_j and $(\Delta A)^2_{\rho_0} = \langle A^2 \rangle_{\rho_0} - \langle A \rangle^2_{\rho_0}$ with respect to a state ρ_0 of the system that has to be guessed. In the best case information about the estimated state is known and plugged in here, otherwise a complete mixture can be used. This would correspond to no knowledge on the state at all. From these formulas an expression for optimal c_j for a set of given A_j can be cast. To minimize the uncertainties with respect to the A_j, an equal distribution on the Bloch Sphere should be chosen. Alternatively a random set will work as well, but the errors will increase[40]. An example distribution is plotted in figure 3.2 where each point on the surface of the Bloch Sphere marks the intersection of a measurement axes of the form $A = x \cdot \sigma_x + y \cdot \sigma_y + z \cdot \sigma_z$. The continuous line is an example where 2 endpoints are connected. Because the same basis is measured on all qubits, it can be visualized on the Bloch Sphere of a single qubit. Together with the set of c_j's the state can be reconstructed. In the later performed 6 qubit tomography, the c_j's form a tensor of dimension 28x83. The index j fixes the first dimension, the second depends on possible combinations of $k+l+m$. There is a block of values for $k+l+m = N$, a block for $k+l+m = N-1$, for $k+l+m = N-2$ etc until $k+l+m = 1$ is reached. In Matlab, the following code will calculate this number.

```
dim = 0;
for i=NQubits:-1:1
        dim = dim + nchoosek(i+2,i);
end
```

The above described blocks are iterated for "NQubits" qubits in the system and the number of possible distributions is summed up. The function nchoosek(n,k) calculates $\binom{n}{k}$. In the case for NQubits=6, the result will be 83. This is also the number of $\langle \left(X^{\otimes k} \otimes Y^{\otimes l} \otimes Z^{\otimes m} \otimes 1^{\otimes n} \right)_{PI} \rangle$ type expectation values that are calculated and describe unique correlations from which the density operator is calculated. Full tomography would use 3^N ($= 729$ for 6 qubits) correlations and therefore more measured values contribute to individual entries in the density matrix. This is quantified in appendix B and shows that indeed the average number of values for an entry is lowered by a factor 5.44 compared to Full Tomography.

Table 3.1 gives the results from[40] for a 4 qubit measurement and illustrates the behaviour of PI tomography with an optimized and random set to a full tomographic measurement. Although the fidelity is smaller for both PI schemes, the optimized version achieves good results.

Overlap with with the symmetric subspace

Any tomography is performed to gain information about an previously unknown state but PI tomography requires the state to be PI symmetric. With the relation

$$P_s^{(6)} \geq \frac{2}{225}\left(J_x^2 + J_y^2 + J_z^2\right) - \frac{1}{90}\left(J_x^4 + J_y^4 + J_z^4\right) + \frac{1}{450}\left(J_x^6 + J_y^6 + J_z^6\right) \tag{3.9}$$

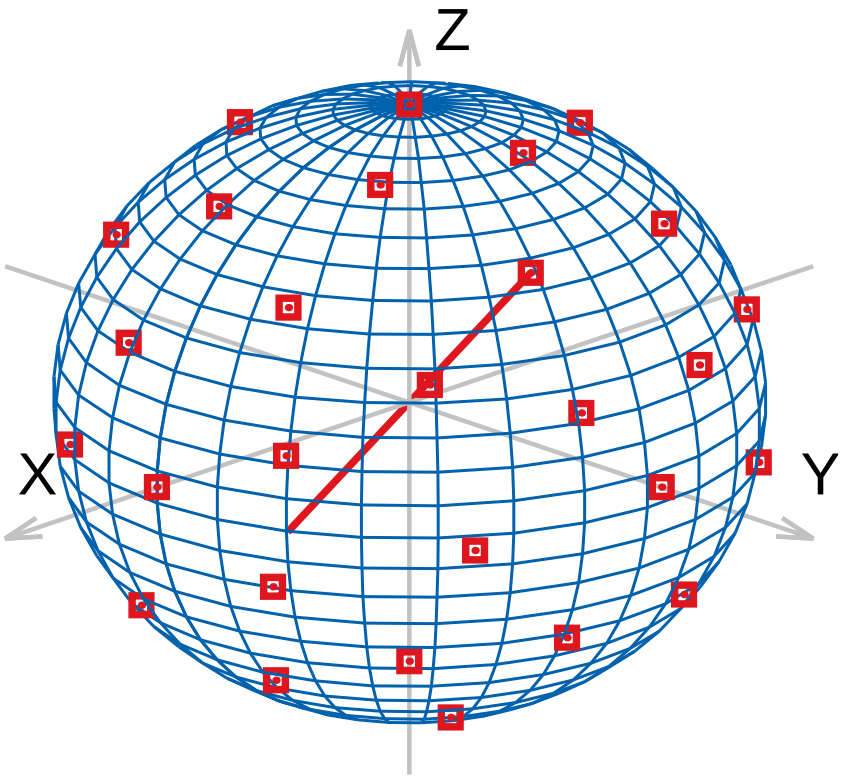

Figure 3.2: Distribution of the directions A_j from equation 3.7 for a 6 qubit PI tomography with 28 settings. The red marks denote the endpoints of measurement axes, one example is drawn (endpoint on the back side not shown). The coordinates give the superposition of the x,y and z-direction. This plot is optimized and includes a pure σ_x, σ_y and σ_z measurement.

Tomographic Scheme	Fidelity compared to ideal $\mathcal{D}_4^2$
Full Tomography	0.873 ± 0.005
PI Tomography with an optimized set	0.852 ± 0.009
PI Tomography with random set	0.814 ± 0.059

Table 3.1: Comparison of the reconstructed density matrix of the $\mathcal{D}_4^2$ symmetric Dicke State via different tomographic schemes to the theoretical state from [41]. Random settings give the same result within the errors of the optimized measurement, but have larger errors themselves.

an estimation to the overlap with the symmetric subspace can be made. $J_x = \frac{1}{2}\sum_k X_k$, $J_y = \frac{1}{2}\sum_k Y_k$ and $J_z = \frac{1}{2}\sum_k Z_k$ and X_k are the σ_x operator on the kth qubit[5]. The space is the one of the symmetric Dicke State[11], that will be introduced later. Values of the J_i can be extracted from measurements along the X,Y and Z-direction on all qubits. A derivation of the exact relation is done in appendix A.

To use this estimation, 3 measurement directions have to be fixed but fortunately PI Tomography gives some freedom in choosing the A_j in eq. 3.7. Finding a set of measurement directions that includes X,Y and Z is then straightforward and the recorded data can be used for the state reconstruction as well.

With the good performance for 4 qubits, good result can be expected for a state reconstruction of 6 qubits. Comparison with data from a full tomography will not be possible, because the time to collect sufficient statistics on all $3^6 = 729$ settings would reach $\approx$ a month of 24h 7 days a week measurement. PI tomography only requires 28 settings and will therefore reduce the time to $\approx$ 20h. (The values refer to the experiment described later)

PI Tomography	Full Tomography
reconstructs only the permutationally invariant part of the state	reconstructs the full state
time and data scale with $\propto N^2$	time and data scale with $\propto 3^N$
measurement bases can be chosen in different ways	measurement bases can be chosen in different ways
the same base is measured locally on all qubits	different bases are measured locally on the qubits
Equal distribution of the measured data over the density matrix with comparable low average	Fluctuating distribution of the measured data over the density matrix. Clear patterns are visible but the average number of contributions is by a factor 10 higher than for PI Tomography
Reconstructed state might not be physical	Reconstructed state might not be physical

Table 3.2: Comparison of the features of PI Tomography and full tomography

Table 3.2 gives a summary of features for both tomographic methods. The last point is important if the matrix is further used in calculations because an unphysical density

[5]for example $X_k = (\mathbb{1})_1 \otimes (\mathbb{1})_2 \otimes \cdots (\sigma_x)_k \cdots \otimes (\mathbb{1})_N$ when the index labels the qubit number

matrix can lead to unreasonable result in some measures. Reconstructed stays for a direct use of formulae 3.2 and 3.7 with the recorded values and without taking any statistics into account.

4 Maximum Likelihood Estimation

To extract a physical, in the sense valid in calculations, result from the data, the extracted state is fitted to the nearest physical state. Physical means the density matrix is normalized, hermitian and positive. The core component is the likelihood function[21], which gives a measure how close a measured density matrix is to the requirements. The only task then is to minimize this function with standard minimization tools. In this experiment the approach by James et al. is used [22], where the matrix is formed in different steps. His approach is sketched in the following.

- To account for non negativity, $\rho = T^\dagger T$ must hold
  Proof: $\langle\psi|T^\dagger T|\psi\rangle = \langle\psi'|\psi'\rangle \geq 0$
  This results in non-negative entries on the diagonal of the matrix.

- This construction is also hermitian
  Proof: $\rho^\dagger = \left(T^\dagger T\right)^\dagger = T^\dagger \left(T^\dagger\right)^\dagger = T^\dagger T = \rho$

- Normalization is ensured by dividing by trace

$$\varrho = \frac{T^\dagger T}{\mathrm{Tr}\left[T^\dagger T\right]}$$

A general density matrix has $4^N - 1$ free parameters that must be found. To make the matrix optimizable, a diagonal form is chosen, where the upper right part of the matrix is zero. For a 2 qubit example the matrix reads

$$T\left(\vec{t}\right) = \begin{pmatrix} t_1 & 0 & 0 & 0 \\ t_5 + it_6 & t_2 & 0 & 0 \\ t_{11} + it_{12} & t_7 + it_8 & t_3 & 0 \\ t_{15} + it_{16} & t_{13} + it_{15} & t_9 + it_{10} & t_4 \end{pmatrix}$$

but can be extended to an arbitrary number. There are 16 parameters here but only 15 are free to choose when normalization is considered. So the matrix is

$$\rho_P(\vec{t}) = \frac{T^\dagger\left(\vec{t}\right) T\left(\vec{t}\right)}{\mathrm{Tr}\left[T^\dagger\left(\vec{t}\right) T\left(\vec{t}\right)\right]}$$

and the elements, that have to be found during optimization, are the entries of the vector $\vec{t}$. In the experiment counts from the detectors are recorded, for whom a Gaussian probability distribution is assumed. Ideally a function recreating the noise behaviour of the used detectors and setup should be used. The probability to obtain a set of $\{n_i\}$ counts then is

$$P\left(\{n_i\}\right) = \frac{1}{N_{norm}} \prod_{\nu} \exp\left[-\frac{\left(n_\nu - \bar{n}_\nu\right)^2}{2\sigma_\nu^2}\right]$$

The σ_ν are the standard deviations for the νth record, that can be approximated by $\sqrt{\bar{n}_\nu}$, and N_{norm} is normalization constant. The expected counts have a connection to the state, described by a density matrix

$$\bar{n}_\nu\left(\vec{t}\right) = \mathcal{N}\langle\psi_\nu|\rho_P\left(\vec{t}\right)|\psi_\nu\rangle$$

with $\mathcal{N}$ being the total number of counts. So the full expression for the probability gives

$$P\left(\{n_i\}\right) = \frac{1}{N_{norm}} \prod_{\nu} \exp\left[-\frac{\left[\mathcal{N}\langle\psi_\nu|\rho_P\left(\vec{t}\right)|\psi_\nu\rangle - n_\nu\right]^2}{2\mathcal{N}\langle\psi_\nu|\rho_P\left(\vec{t}\right)|\psi_\nu\rangle}\right]$$

Numerically it is equivalent to maximize $P\left(\{n_i\}\right)$ or minimize its logarithm, to one has to find the minimum of

$$\mathcal{L}\left(\vec{t}\right) = \sum_{\nu} \frac{\left[\mathcal{N}\langle\psi_\nu|\rho_P\left(\vec{t}\right)|\psi_\nu\rangle - n_\nu\right]^2}{2\mathcal{N}\langle\psi_\nu|\rho_P\left(\vec{t}\right)|\psi_\nu\rangle}$$

for a specific $\vec{t}$. This function is called the likelihood function. The programmatic implementation is a multivariate optimization in terms of the components of $\vec{t}$.

Although a state with a small $\mathcal{L}$ can be found, its form depends on the used algorithm. For instance an algorithm that will not lead into the global optimum will produce a different than an algorithm that reaches the optimum. It must be assumed, that the state that is directly calculated from the counts lies somewhere in the vicinity of the "real" state and we hope that the above algorithm will lead to it. Unfortunately there is no guarantee for that. Extracted density operators can be used for calculations but merely by construction.

A more fundamental problem is the probabilistic interpretation of the recorded data[3]. This is done via equation 3.1, which converts the recorded events to a value that is later interpreted as probability although it should be used as a frequency. An example would be a dice. To deduct that it is fair, the measurement should record equal counts for each side. But this is only achieved for an infinite number of tries. For finite repetitions one should interpret the results as frequency not as absolute probability, because shifted occurrences of each side due to normal fluctuations must be seen as unequal weights for the sides. More severe are the impacts for events that are very unlikely in the system and might not generate an amplitude in the measurements within the time of the experiment. The problem then is that the reconstruction (eq. 3.2) as well as the MLE method do not account for this and will treat a small probability to be exactly equal to zero and therefore might not reproduce

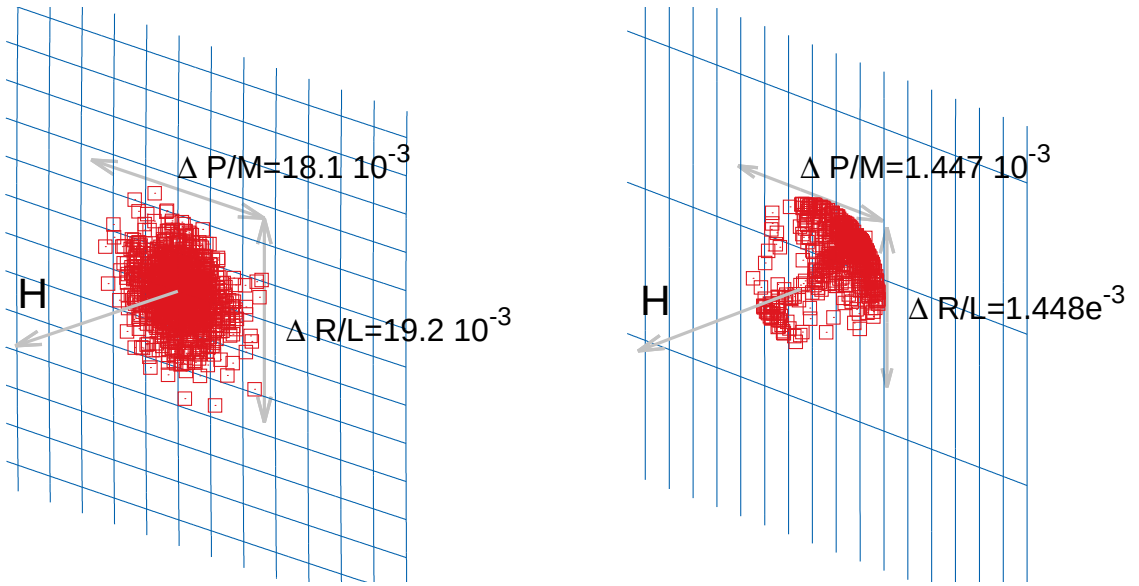

(a) Scattering due to Poisson statistics

(b) Scattering due to different starting vectors $\vec{t}$

Figure 4.1: Simulated 1 qubit tomographies with 1000 iterations, for the state $A\left(|H\rangle + 0.001|P\rangle + 0.001|R\rangle\right)$. A is the normalization constant, the additions of $|P\rangle$ and $|R\rangle$ prevent the unphysical zero probability in the calculated count rates. In a) the simulated counts are perturbed by a Poissonian distribution for each iteration, the starting values for $\vec{t}$ are fixed and the resulting state is plotted on the Bloch sphere (blue). The width of this scattering scales with the number of iterations. In b) no statistic is applied, but the starting $\vec{t}$ is randomized. The radius does not scale with the number of iterations

the correct state. Methods like *Hedged Maximum Likelihood Estimation* can circumvent such effects e.g. by introducing a default minimal probability[2]. However for analyzing a measured state and to give an estimate what was actually measured, the standard MLE method is sufficient but it is important to keep potential problems in mind when using the results.

Figure 4.1 shows reconstructed 1 qubit states on the surface of the Bloch Sphere to visualize different effects of the MLE method. The algorithm takes an ideal state, calculates the expected probability to detect certain polarizations, applies noise through a poissonian distribution to[1] the expected number of events and reconstructs the density matrix with the MLE algorithm. For best results, the state $|\psi\rangle = N\left(|\mathrm{H}\rangle + 0.001|\mathrm{P}\rangle + 0.001|\mathrm{R}\rangle\right)$ is used. This is done to eliminate events that are calculated to be zero, but can have contributions due to imperfections in the setup or noise in the detectors. For example the event to detect $|\mathrm{V}\rangle$ is expected to be exactly zero, but noise in the detectors can give several counts through noise. Calculating the Poissonian distribution $f(k, 0)$ gives again zero, so the result does

[1] The distribution reads $f(k, \lambda) = \frac{\lambda^k e^{-\lambda}}{k!}$. λ is taken as the number of counts in the channel to be randomized.

not reflect a real experiment. This is why a state with small admixtures is chosen.

The plots show different types of scattering in the reconstructed states. First, there is scattering that results from the applied statistic, and there is scattering depending on how the start values of the afore described $\vec{t}$ vector are chosen. Figure 4.1a shows endpoints after MLE when poissonian noise is added and $\vec{t}$ is kept fix for each run. Compared to the state vectors that were not optimized through MLE, the overall distance to the ideal state decreases so the recovered state is on average closer to the original one than the perturbed measured. This shows that MLE helps to recover a state that is subject to noise. Figure 4.1b shows result where the state was not perturbed by any statistic on the counts but the starting parameters for the vector $\vec{t}$ are randomized. The overall spread is smaller by a factor 10 compared to the first plot so this effect will have neglectable impact but it illustrates the dependence of the result on input parameters in the MLE algorithm.

The simulations demonstrate that fitting a state with the above method has effects on the recovered state. Despite the previously mentioned problems of the probabilistic interpretation the routine is able to move *all* directly (unfitted) state vectors closer to the "real" state, thus creating an improvement over states that are reconstructed without any optimization. There are other approaches that try to eliminate the remaining flaws, but so far the relatively simple assumptions and easy formulation make the MLE approach the tool of choice.

5 Experiment

In this part the experimental setup and the underlying processes to create and measure the 6 qubit symmetric Dicke State are explained.

5.1 Entangled State Production via Spontaneous Parametric Down Conversion

The basic process exploited to create entangled photons is Spontaneous Parametric Down Conversion (SPDC). Descriptions of this process were first published by Madge and Mahr [29] and more elaborate by Byer and Harris [9]. In a nonlinear crystal an incoming photon with energy $\hbar\omega$ can split in 2 photons with half the energy that have a fixed polarization relation and are therefore entangled. Depending on the crystal type and orientation, different types of polarization and emission directions can be constructed.

Any electromagnetic field inside a nonlinear crystal will induce a local polarization of the form [43]

$$P = \epsilon_0 \left(\chi^{(1)} E + \chi^{(2)} E^2 + \chi^{(3)} E^3 + \cdots\right)$$

with the permittivity ϵ_0 and $\chi^{(n)}$, the nonlinear susceptibility of order n in the medium. Depending on the incident power and the type of material, higher order $\chi^{(n)}$ will contribute. If the standard ansatz for an electric field $E(t) = A\cos(\omega t)$ is inserted, the polarization up to second order in χ becomes

$$P(t) = \epsilon_0 \chi^{(1)} A \cos(\omega t) + \frac{1}{2}\epsilon_0 \chi^{(2)} A^2 \left[1 + \cos(2\omega t)\right]$$

Considering the field in a quantum mode description, the expression shows that a field of frequency ω will create another field with frequency 2ω. The first one (later called pump field) will induce local movements of charges which will produce the second field, that can be detected as 2 photons in the distance. The nonlinearity can also be used to generate photons of defined frequencies in up- or down-conversion. Artificially imposing 2 fields, the creation of photons that have the sum or difference in frequency can be stimulated[35].

In this setup light with 390 nm wavelength will be used to create entangled photons of 780 nm, so just a single pump field is injected in the crystal. In this case, down conversion happens randomly what gives raise to the "spontaneous" in SPDC. In terms of photons, a

single one of frequency ω_p (pump), will decay in 2 photons with frequency ω_s (signal) and ω_i (idler)[1]. Energy conservation must hold

$$\omega_p = \omega_s + \omega_i$$

as does momentum conservation

$$\vec{k}_p = \vec{k}_s + \vec{k}_i \tag{5.1}$$

The second requirement is also a phase matching condition that needs to be fulfilled to have output at all[43]. Eventually the centers of 2 creation processes are separated by odd multiples of the wavelength, that would correspond to a phase difference of π, so no resulting field exits the crystal. Any other phase difference than 2π between creation centers will average out the overall fields. Thus it is mandatory to have the signal and idler photons phase matched. Using $\left|\vec{k}\right| = \frac{\omega n}{c}$ the expression

$$n_p - n_s = (n_i - n_p)\,\frac{\omega_i}{\omega_s} \tag{5.2}$$

can be found. Commonly the refractive index is a function of the frequency $n_i = n\,(\omega_i)$ and for the case of normal dispersive media $n_i \leq n_s \leq n_p$ holds. This shows that $(n_p - n_s) \geq 0$ and $(n_i - n_p) \leq 0$. Therefore there is no general solution to 5.2. There are crystals hat have an increasing refractive index for lower frequencies but due to large energy losses the common method is to use birefringent crystals. In the simplest type, the refractive index differs only for a single propagation direction. This axis is called the optical axis and light propagating in this direction experiences the *extraordinary refractive index*, whereas light in the perpendicular plane is subject to the *ordinary refractive index*. There is a discrimination between uniaxial positive ($n_e > n_o$) and uniaxial negative ($n_e < n_o$) crystals. The pump photon must be polarized along the direction with the lowest refractive index. In case signal and idler photon have the same polarization, the phase matching scheme is called Type I, if they are orthogonal polarized Type II.

Birefringence requires phase matching (eq. 5.1) for all 3 propagation directions separately. E.g. $\omega_p n_p \vec{k} = \omega_i n_i \vec{k} + \omega_s n_s \vec{k}$ must hold for any $\vec{k} \in \left\{\vec{k}_p, \vec{k}_s, \vec{k}_i\right\}$. Calculations show that the emission of signal and idler photon for Type II phase matching (which is used here) is only fullfilled if the emission lies on 2 cones[43](see figure 5.1). Aperture and center can be influenced by the angle of the crystal relative to the pump beam. Tilting, also called *angle tuning*, allows fine adjustment of the matching condition. If the only intersection is a single line, the setup is called *collinear*, configurations with 2 intersections are called *non-collinear*. Because the signal photon is emitted on the surface of one cone, the idler on the other, collecting the light that the intersection of both will result in an entangled state of the type

$$\frac{1}{\sqrt{2}}\left(|\mathrm{HV}\rangle + e^{i\phi}|\mathrm{VH}\rangle\right)$$

[1] The nomenclature has historical reasons

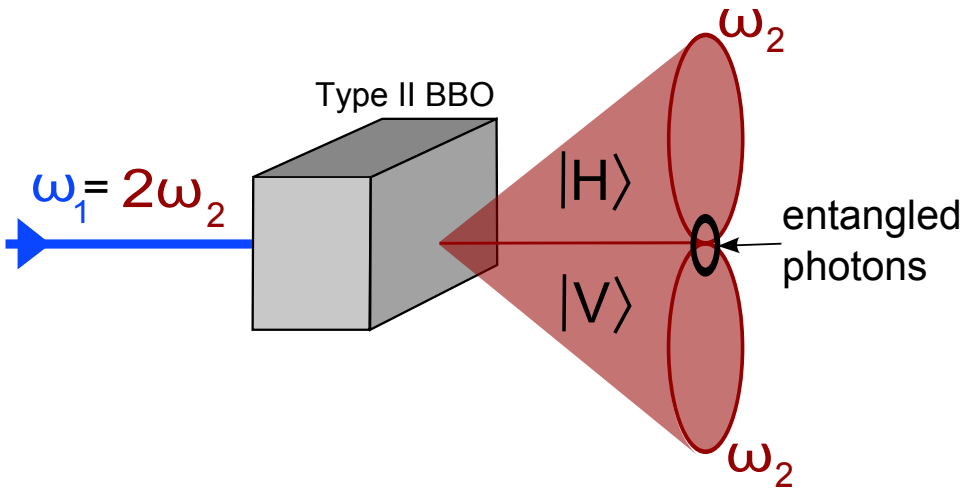

Figure 5.1: Emission cones of Type II spontaneous parametric down conversion in a collinear setup for a β-Barium-Borate (BBO) crystal.

for Type II ($\frac{1}{\sqrt{2}}\left(|\mathrm{HH}\rangle + e^{i\phi}|\mathrm{VV}\rangle\right)$ for Type I). In the used setup, a BBO crystal in Type II collinear orientation produces entangled photons that are used as the basic unit to build the desired symmetric Dicke State. Schematics of this configuration is shown in figure 5.1 . The next section will describe the formation of the genuine 6 photon entangled Dicke State.

A small remark to effects of the polarization depended refractive index in the crystal: Because of the nonlinearity in the crystal, different polarized light will propagate differently[26]. This effect is called *walk of effects*. Emission cones in the far field will have different shapes and wall thicknesses resulting in an asymmetric overlap. Thinner crystals will show less walk off effects, because the propagation distance in the nonlinear medium is decreased, but likewise the interaction and therefore production region is reduced. In the used configuration, the crystal thickness is chosen to be 1mm. To compensate the different wall thicknesses as much as possible, angle tuning is used. A maximum in 2 fold coincidences in the linear setup, after the fiber (see figures 5.7 and 5.2), corresponds to a maximum in the overlap of both cones at the fiber tip.

5.2 The Symmetric Dicke State

The symmetric *Dicke State*[11, 42, 39] is the sum of all possible permutations of m spin $\frac{1}{2}$ particles with j excitations. This state that will be created and observed. The excitation can be spin up, compared to spin down of the Rest of the members or different polarization directions. In the case of the photonic system studied here, excited qubits are horizontally polarized ($|H\rangle$), not excited are vertically polarized ($|V\rangle$). The formal definition reads

$$\mathcal{D}_m^j = \begin{pmatrix} j \\ m \end{pmatrix}^{-\frac{1}{2}} \sum_i P_i \left(|H\rangle^j \otimes |V\rangle^{(m-j)}\right) \tag{5.3}$$

where $\{P_i\}$ are all permutations of the expression in the brackets and $|H\rangle^n = |H\rangle^{\otimes n} = \underset{n}{\otimes}|H\rangle$. In this experiment, the state $\mathcal{D}_6^3$ will be crate and observed. Its terms have he polarization configurations

HHHVVV	HHVHVV	HHVVHV	HHVVVH
HVHHVV	HVHVHV	HVHVVH	HVVHHV
HVVHVH	HVVVHH	VHHHVV	VHHHVV
VHHVHV	VHHVVH	VHVHVH	VHVVHH
VVHHHV	VVHHVH	VVHVHH	VVVHHH

It is chosen, because a loss of photons is not equivalent with the loss of entanglement, and common other states, like the W-state or GHZ state can be created by local projections[13]. This allows a general experiment that can easily been expanded to other states.

5.3 Production of a Symmetric Dicke State

In section 5.1 the basic process to create a pair of entangled photons via Type II collinear SPDC was presented. The symmetric Dicke state $\mathcal{D}_6^3$ contains a total of 6 qubits. This is only possible if 3 pump photons split into 6 down converted ones at the same time, or at least within the coherence length of the laser. This ensures that they are indistinguishable by their production time. Interaction between the light field and the crystal is described by the hamiltonian

$$\mathcal{H} = i\hbar\kappa a_H^\dagger a_V^\dagger + h.c.$$

where $a_{\{H,V\}}^\dagger$ is the creation operator for a horizontal or vertical polarized photon and κ is the coupling of the field to the crystal. Interaction is modeled by the time evolution operator for an interaction time of t

$$|\psi(t)\rangle = U(t)\,|\text{vac}\rangle = \exp(-i\mathcal{H}t)\,|\text{vac}\rangle$$

The time dependent state is worked out in [46] and reads

$$|\psi(\tau)\rangle = \frac{1}{\cosh(\tau)} \sum_{n=0}^{\infty} \tanh^n(\tau)\,|n_H, n_V\rangle \tag{5.4}$$

with the interaction parameter $\tau = \kappa t$ instead of the time and $|n_H, n_V\rangle$ denoting a state with n horizontal and n vertical photons. The important factor to estimate the production rate is $\tanh^n(\tau)$ for the n photonic state. The used crystal has a thickness of 1mm, so $\tau \ll 1$ is justified and therefore $\tanh(\tau) \approx \tau$. The count rate then will be $\propto \tau^{2n}$ and in terms of the underlying field-crystal interaction $\propto \left(|E|\,\chi^{(2)}\right)^{2n} \propto P^n$ where $P = |E|^2$ is the

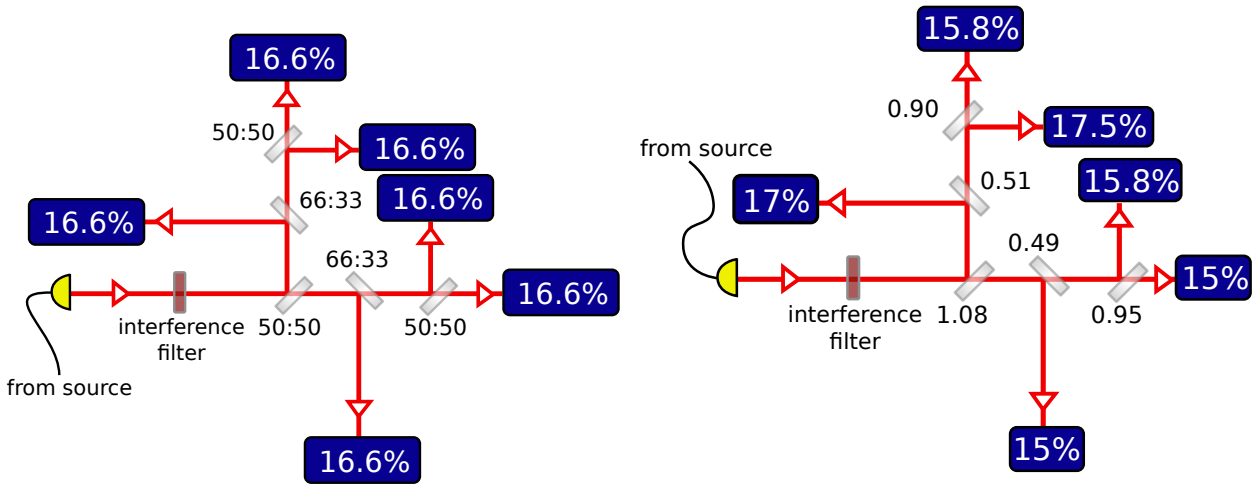

(a) Ideal splitting ratio

(b) Measured splitting ratio in the experiment.

Figure 5.2: Linear setup to prepare the Symmetric Dicke State in its ideal and real form. From the source a bunch of 6 entangled photons is fed into the setup. The (ideal) polarization independent beam splitters distribute equal beam intensity into each arm. For the case that each photon splits into a different arm, the state can be observed. The trigger is a simultaneous photon event in each of the blue analysis blocks. a) shows the ideal splitting ratio with an expected intensity of 16.6% of the original in each arm. b) shows the measured splitting ratios and intensity distributions. $33 : 66 = 0.5$ and $50 : 50 = 1$ would be expected; overall 3.73% are lost.

power of the field inside the crystal. More power will help dramatically. For example an increase of the power by 1% will result in 6% higher production rates, 2% in 12% more and so on; the high exponent has a big impact here.

To observe the Symmetric Dicke State, the 6 photons that form the state have to be separated spatially, otherwise the above described tomographic scheme would not be applicable, as local measurements are not possible. In addition the coherence length must be longer than the depth of the crystal, that the place of production cannot be resolved[24]. This is achieved by a narrow bandgab filter that reduces the uncertainty of the wavelength and increases the coherence length.

Spatial separation is realized through probabilistic splitting of light from the source in separated arms. Such a setup is called a *linear optical setup*. In the case of 6 qubits, 6 arms are needed as illustrated in figure 5.2a . Ideally, the beam splitters are polarization maintaining and distribute equal intensity ($16.\bar{6}\%$) into all arms. This is achieved with 3 50:50, and 2 33:66 splitters. A Field Programmable Gate Array (FGPA) counts concurrent events in the arms. If 6 photons were detected simultaneously in all arms, the event can be counted to be a 6 photon event. This method is called post selection, because more data are recorded than used. For example all 4 fold events are stored as well but discarded in the evaluation. Also, all arms must have the same length, because otherwise

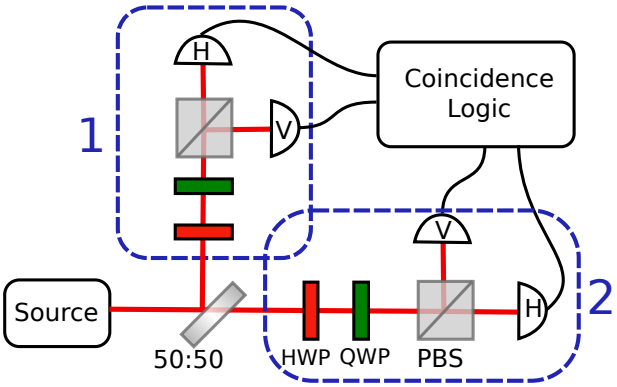

Figure 5.3: Analysis of a 2 qubit state. If a photon is detected in arm 1 and 2 simultaneously, a 2 photon state has been detected.

photons entering the setup concurrently, will be detected at different times, destroying the 6 fold event pattern. To extract probabilities of the type $P_{|XYZXYZ\rangle}$, the counts from the FPGA are used. An example wiring for 2 qubits is shown in figure 5.3. The part that is highlighted by blue surroundings is an analysis block like in 5.3. In the example, possible counts originate from HH, HV, VH and VV events for which $P_{|HH\rangle}$, $P_{|HV\rangle}$, $P_{|VH\rangle}$ and $P_{|VV\rangle}$ can be calculated. For an arbitrary state of N qubits, 2^N coincidence combinations are possible.

A downside of the linear setup is its efficiency in distributing the photons "correctly". From the produced packs of 6 photons, only $\frac{6!}{6^6} \approx 1.54\%$ can be detected via coincidences of exactly one photon in each arms. But this is only true for an ideal setup. Beam splitter may not be 100% polarization maintaining or do not split the beam in the expected ratio. This will reduce the effective splitting even further. The measured intensity distribution is shown in figure 5.2b. Every splitter was tested on its performance and the best used. Figure 5.4 shows the example curves for 2 elements, later used in the setup. There are derivations from a perfect 50:50 splitting as well in polarization dependence, but within acceptable values.

The combined event rate is then calculated via

$$e_N \propto \tau^N f \, \eta_{\mathrm{Det}}^N \, p_N \tag{5.5}$$

with τ^N the production rate in the crystal, η_{Det}^N the detection efficiency of the detectors (60%), p_N the probability to distribute the photons correctly (the above 1.54%) in the linear setup and f, the repetition frequency of the pulsed laser (80.8Hz). From recorded event rates, the proportionality factor within τ can be calculated and then the estimated event rate for higher or lower order events extrapolated.

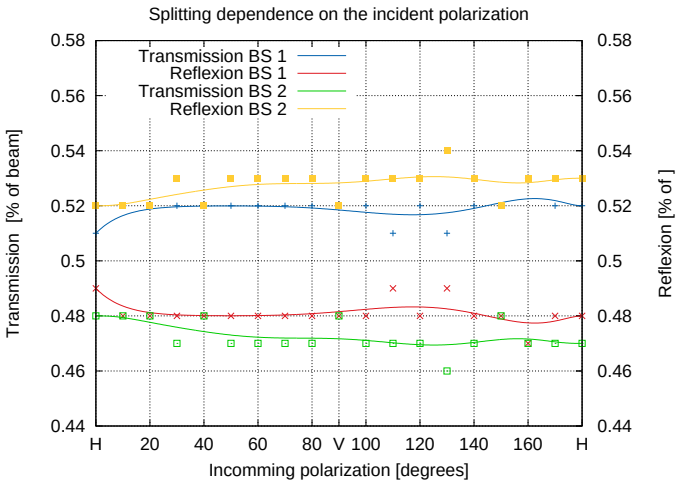

Figure 5.4: Transmission and Reflexion of the first beam splitter in 5.2 and another sample from the same batch for different incident polarizations. Although the splitting is not ideal 50 : 50, the polarization is preserved. The differences between the 2 samples are small but the ones used in the setup are chosen to be the best in terms of polarization stability and splitting ratio.

5.4 Higher order noise of $\mathcal{D}_6^3$

Noise can be produced by imperfections in the detectors that lead to counts when no photon was present or a photon was present but no event was triggered. In case of symmetric states, a special type is produced through loss of photons. Formula 5.4 shows that the number of photons in a produced state depends on the laser power inside the crystal. Besides 2 fold states, also 4,6,8 etc. ones are created, although with much lower probability.

Eventually an originally 8 fold event looses 2 photons on the way to the detectors and 6 are detected. The big advantage of symmetric Dicke States is that entanglement is not fully destroyed if photons are lost. Figure 5.5 shows possible loss pattern for a 8 fold Dicke state and the probabilities for the different paths. The resulting mixed state is

$$\left(\mathcal{D}_6^3\right)_{noisy} = p \cdot \mathcal{D}_6^3 + (1-p)\left[\frac{4}{7}\mathcal{D}_6^3 + \frac{3}{14}\left(\mathcal{D}_6^2 + \mathcal{D}_6^4\right)\right] \tag{5.6}$$

where the parameter p describes the amount of the "original" $\mathcal{D}_6^3$ state that reaches the detection part from the crystal. Because Dicke States with different number of excitations are orthogonal on each other

$$\langle \mathcal{D}_6^i | \mathcal{D}_6^j \rangle = 0 \quad \forall i \neq j \tag{5.7}$$

the density matrices for states of different j's have no entries in common. This allows an estimate of the *noise parameter* p. Density operators of pure $\mathcal{D}_6^{\{2,3,4\}}$ states have the same amplitude in every nonzero element; $0.066\bar{6}$ for $\mathcal{D}_6^2$ and $\mathcal{D}_6^4$, 0.05 for $\mathcal{D}_6^3$. Figure 5.6

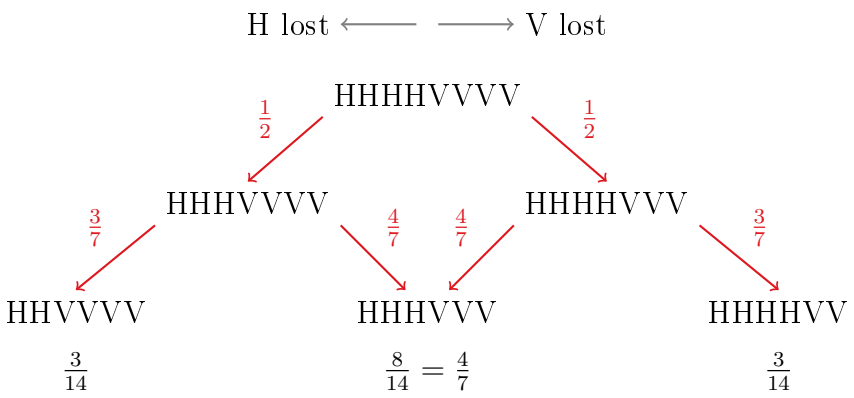

Figure 5.5: Loss scheme for the D_8^4 to the D_6^3 state. The fractions over the arrows and under the last line of nodes show the splitting ratio in the corresponding path or state.

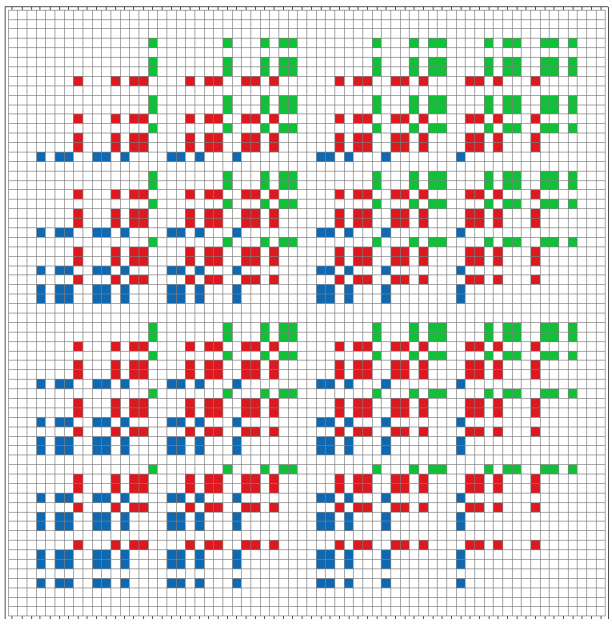

Figure 5.6: Density operator entries that solely originate from $\mathcal{D}_6^2$ (blue), $\mathcal{D}_6^3$ (red) or $\mathcal{D}_6^4$ (green) in a mixed state of the 3. Each square represents an entry of the matrix.

illustrates this in a color plot. Each spare is an entry in the 64x64 density operator. Blue squares are part of $\mathcal{D}_6^2$, red ones of $\mathcal{D}_6^3$ and green ones of $\mathcal{D}_6^4$. There is no common entry. Measured matrices show alternating heights in elements that have equal ones in reality. For reliable estimations of p the green and blue entries are averaged. Then

$$(1-p)\,\frac{3}{17}\cdot 0.066\bar{6} = \langle \mathcal{D}_6^{\{2,4\}} \rangle \Rightarrow p = 1 - \frac{14\langle \mathcal{D}_6^{\{2,4\}} \rangle}{3\cdot 0.066\bar{6}} \tag{5.8}$$

gives an estimation for average over all elements from $\mathcal{D}_6^2$ and $\mathcal{D}_6^4$. Also elements from $\mathcal{D}_6^3$ can be used. Different power levels inside the crystal should lead to different p parameters, as the 8 photon production rate changes. Although higher laser power will increase the count rate of the desired state, noise will increase as well. Depending on the application, the best mixture must be found.

5.5 Laser System

To increase the power per volume element inside the crystal, there are 2 tricks. First, a pulsed laser source is used to compress the energy of the beam in photon packages. The average laser power will not increase, but the pulses have extreme fields and so the production rate of higher order linear events increases. Second, a resonator where the pulses can circulate and are amplified. The simple picture is, that every time a pulse gets reflected at the entrance mirror, another pulse arrives from the laser system. With this scheme, both will overlap and the overall power in the pulse increases. A bow tie cavity[2] is used (see figure 5.7) . With a continuous wave CW ND:YVO_4 and a mode-locked Ti:Sa resonator (MilleniaX and Tsunami system from Spectra Physics) a 2W cw-equivalent 130 fs pulsed laser beam at 780 nm at a repetition rate of 81 MHz is created. This beam is up converted in an Lithium Triborate (LBO) crystal into a 390 nm UV pulse and injected into the resonator (yellow area in figure 5.7) with a total length of $\approx$ 3.7m. The incoming power of $\approx 500 - 600$ mW is amplified to maximally $\approx 7.5\,W$ of cw-equivalent energy circulating with a BBO crystal placed at the depicted position. Without any disturbance an amplification by a factor 40 to $\approx 21\,W$ of UV power is reachable. Length stabilization is provided by a Hänsch Cuillaud scheme[20]: a small part of the pump light is separated from the beam before the first mirror (mirror IC in figure 5.7) and overlapped with light leaking out of the cavity. If the cavity is stable, both beams have a fixed phase relation, so the light composed of both is linear polarized. If the cavity drifts, a phase shift between both is induced that leads to elliptical polarization. To generate an error signal, the polarization is analyzed by a quarter wave plate and a polarizing beam splitter. For linear polarization both outputs have equal intensity, for circular the intensity shifts. The produced signal can be used to control piezo elements attached to mirrors to keep the length of the cavity constant. Because there are long term drifts as well, 2 piezos are used to account for fast and slower changes. In this scheme, the cavity can stay stable for up to 24h on the highest pump level. Lower power levels are in general more stable and show smaller fluctuations.

[2]The name is lent from the shape of the path the light takes in the setup.

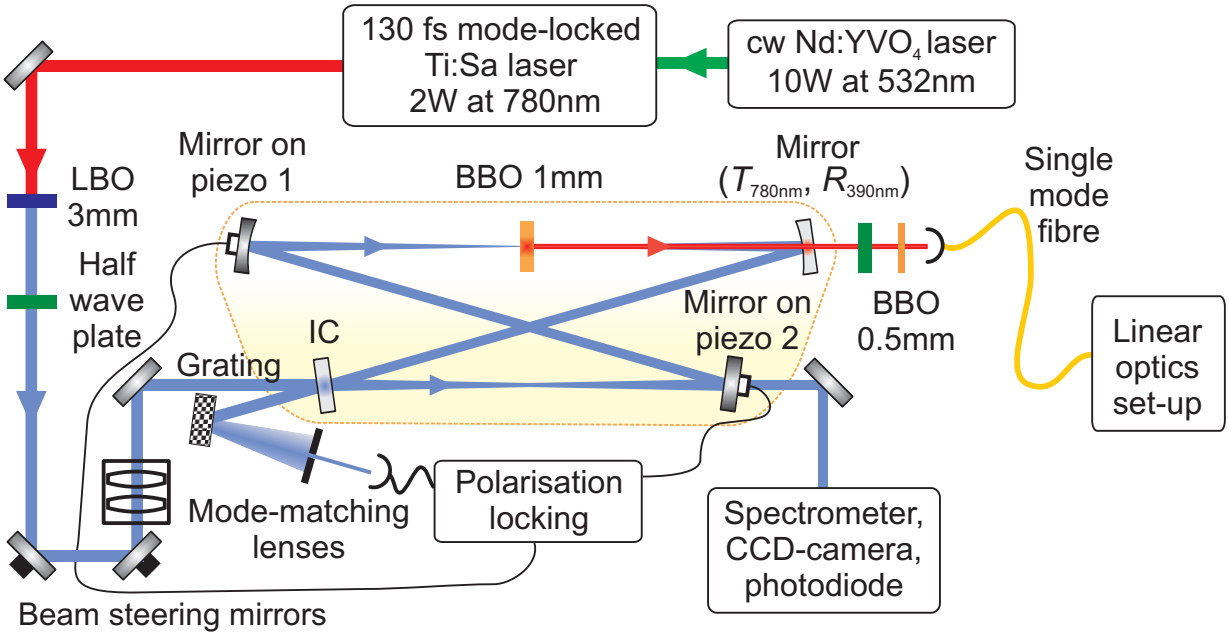

Figure 5.7: Laser system[28] including the pulsed laser source and the resonator (yellow background).

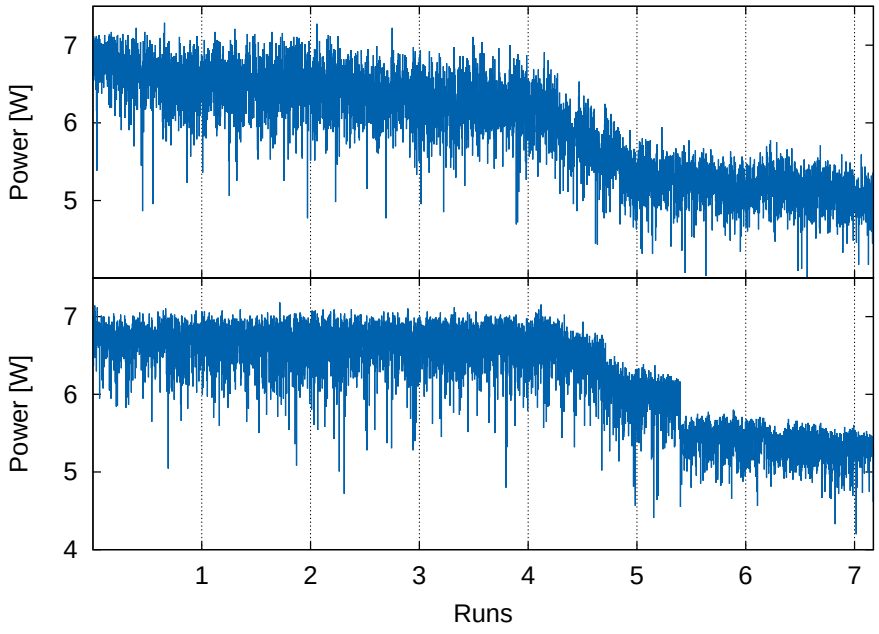

Figure 5.8: Power decrease in power inside the cavity after a measurement time of ≈ 2.7h by the end run 4. The time after which the power decreases and can only be lifted again by moving the crystal is dependent on the incident power.

When operating at high levels, a drop in the power level is visible. Figure 5.8 shows 2 typical degradations, for 2 different measurements at originally 6.5 Watt. After 4 runs[3], which is equivalent to $\approx$ 2.5h of measurement, higher levels can only be reached again by moving the BBO crystal perpendicular to the pump beam. Reusing spots from previous measurement will always lead to low power circulation. This suggests that the field in the crystal caused bleaching, either of the anti reflexion coating or the crystal itself. The repetition rate of 81 MHz and the pulse length of 130 fs produces energies of $\approx$ 617 kW per pulse and therefore longer exposure may cause damage.

The above configuration produces $\approx 14\frac{1}{\text{min}}$ simultaneous events in all arms. This rate is reasonably good tho allow the collection of a tomographic set for permutationally invariant state tomography, but is already too poor for a full tomographic scheme. The previous one can be collected within 24h measurement time, the latter one would require $\approx$ 25 days of 22h measurement time when the same statistic is wanted (in this calculations 500 per basis setting). Rapid decrease in count rate can be seen by an experiment investigating an 8 photonic entangled state produced by SPDC[47]. The used crystal is not placed inside a resonator and the event rate lies around $9\frac{1}{\text{h}}$. The here described setup should be able to produce 8 fold events with a rate of $\approx 3.6\frac{1}{\text{h}}$ if in eq. 5.5 a detector efficiency of 60% is assumed and the altered splitting probability considered.

Due to the previously mentioned degeneration of the exposed crystal spot, a continuous measurement of more than roughly 2.5 hours at 6.5 Watts is not possible. To compensate this, different measurements are combined to one set of data for state reconstruction. To make sure that the resonator is operating in comparable parameters, several criteria are important when joining measurement data:

- The power level and the order of fluctuations have to be equal
- The central UV wavelength inside the cavity has to be the same
- The 2 fold coincidence count rate and
- The 4 fold coincidence count rate have to be equal between the measurements

All this parameters can be adjusted in situ when preparing for the next measurement run. The latter 2 can shift when the coupling into the fiber that leads to the linear setup changes. Reasons could be a deadjustment of the coupler itself but in most cases different locking conditions inside the cavity force minor adjustments. Figure 5.9 shows the Power inside the resonator for a set of composed individual measurements. Count rates from the same measurement run are shown in 5.10 . The points where different measurement runs were joined are barely visible, but a closer look will reveal a small jump at the end of run 4. Later presented density matrices for 6.4 Watt pump power are reconstructed from this measurements.

[3]a run is one circulation through all measurement settings of a tomographic set. In the case of 6 qubits, one run contains 28 measurement directions. Settings are circulated fast compared to the overall measurement time do account for power fluctuations over time.

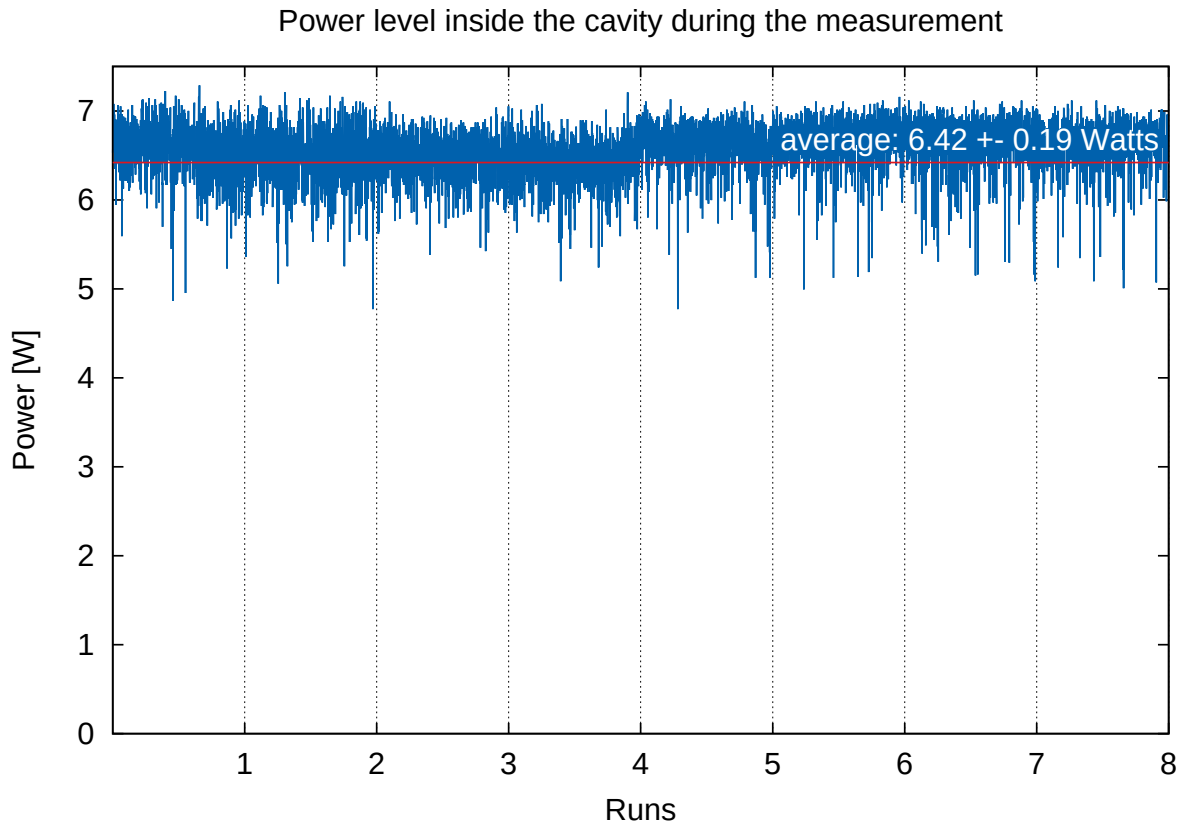

(a) Power inside the cavity for a measurement time of $\approx 20h$

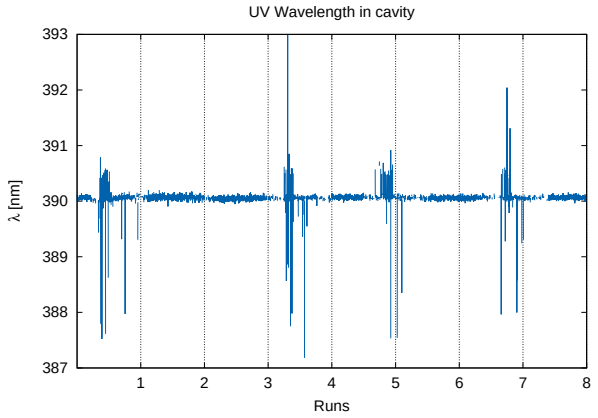

(b) UV Wavelength of the light circulating in the cavity.

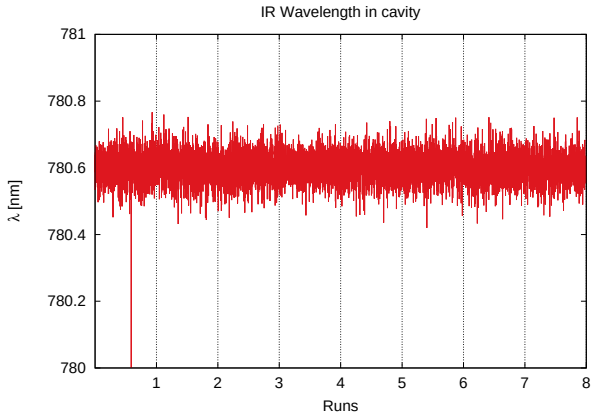

(c) IR wavelength of the light that is up converted to be amplified inside the cavity

Figure 5.9: Power and laser recordings of a 6 qubit tomography measurement. a) shows the power inside the cavity, on average 6.42 ± 0.19 Watts. b) the UV wavelength inside the cavity and c) the IR Wavelength of the light that is converted to UV light in the LBO. A "run" is the measuring of the 28 settings (see eq. **??**) needed for a 6 qubit tomography with a duration of 38 minutes each. The complete measurement took $\approx$ 18h with 507 events per basis and an event rate of $13.11 \frac{1}{\text{min}}$.

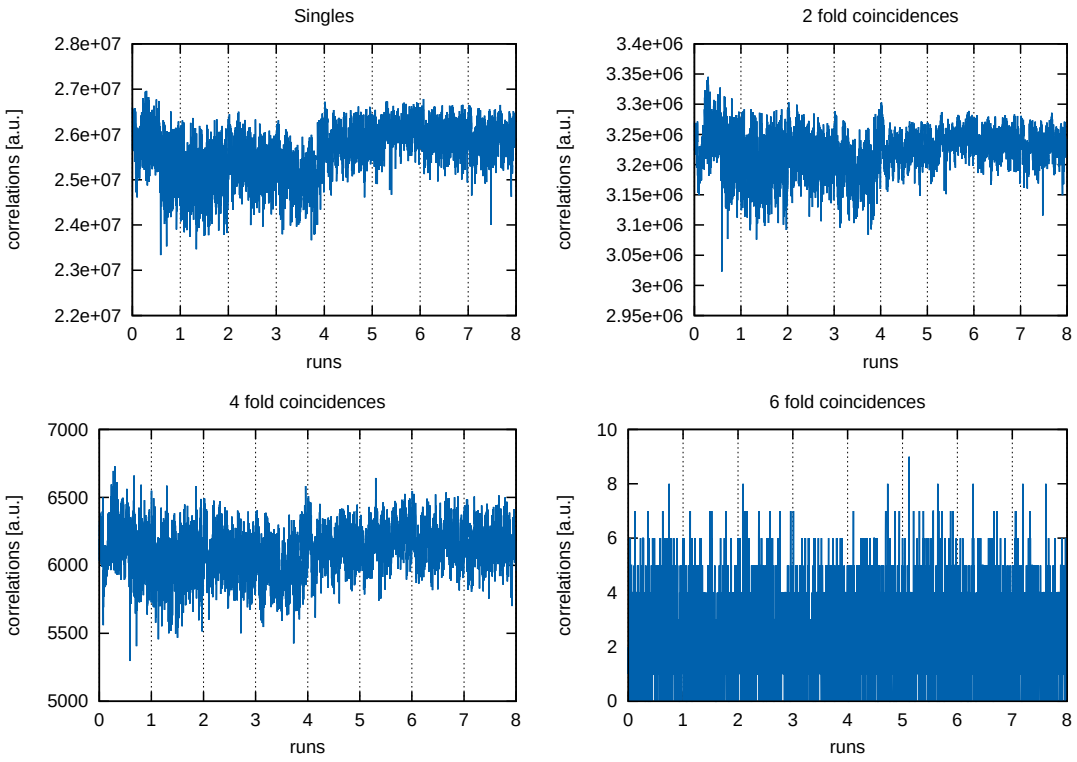

Figure 5.10: Counts of single photons, 2 fold coincidences, 4 fold coincidences and 6 fold coincidences in the 12 detectors of the setup over time. A "run" will take approximately 40 minutes, the graph shows the development of the count rate per minute for the power level shown in 5.9

6 State Tomography of the 6 qubit symmetric Dicke State

This section discusses the results investigating the symmetric Dicke State produced by the described laser system and linear setup. The above explained methods are used to extract the density matrix from measured counts and to compare the observed state to an expected, ideal Dicke State.

6.1 Symmetric Overlap

For PI tomography, a set of 28 measurement directions (see eq. 3.8 and figure 3.2) needs to be measured. To make an estimate on the overlap with the (PI) symmetric subspace of the state, directions $X^{\otimes 6}$, $Y^{\otimes 6}$ and $Z^{\otimes 6}$ are included to make use of eq. 22. In the following, 2 measurements, one at 6.4 the other at 3.7 Watt laser power, are discussed. Their overlap with the symmetric subspace is calculated to be

	overlap
$P = 3.7$ **Watt**	0.9162
$P = 6.4$ **Watt**	0.8868

It is important to note that eq. 3.9 is designed to give 1 for $\mathcal{D}_6^3$ and behave like a distance measure for other states. To be precise, not a general overlap with the (PI) symmetric subspace is calculated, but the overlap with the symmetric subspace of $\mathcal{D}_6^3$. In chapter 5.4 noise that is created from higher order events in the crystal is analyzed. This effects will lead to a mixed Dicke State, which has contributions from $\mathcal{D}_6^2$ and $\mathcal{D}_6^4$. Using eq. 3.9 on these states gives 0.75 each and therefore the estimate for the complete state will decrease. Anticipating results for the amount of noise from chapter 6.4, values of 0.916 for 3.7 Watt and 0.925 for 6.4 Watt are expected. This is in good agreement with the measured one. Because $\mathcal{D}_6^2$ and $\mathcal{D}_6^4$ are PI symmetric, the 28 basis scheme can be used.

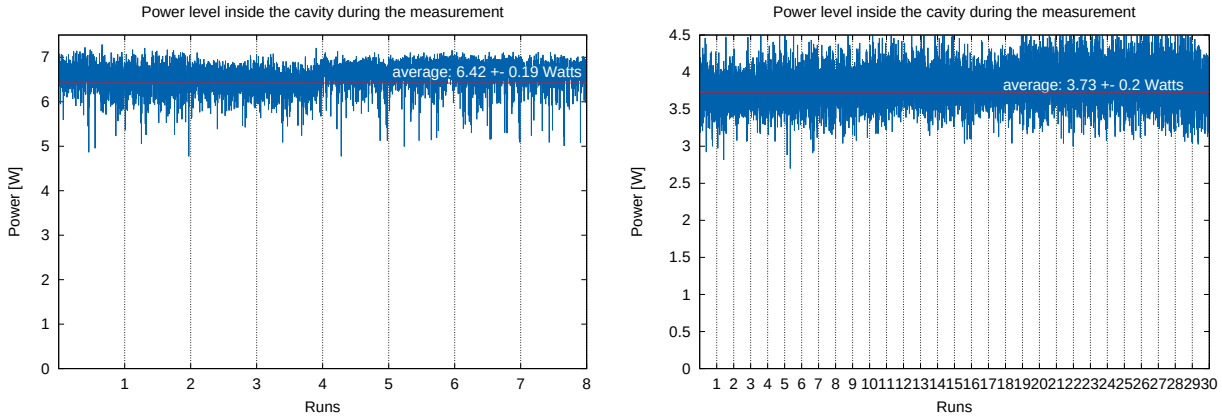

(a) (b)

Figure 6.1: Power inside the cavity for a measurement at a) 6.4 Watts and b) 3.7 Watts

6.2 Reconstructed density matrices

Each of the 28 base settings is measured for 300 seconds (30 measurement points with 10 seconds integration time each), thus it takes 140 minutes to complete one cycle through all of them. Once the last setting is reached, the first one is measured again. This circulation is used to compensate for eventual power fluctuations during the measurement time and will be labeled a "run" in the following graphs on the x axis.

Figure 6.1 shows power levels for 2 composite data sets. For comparison reasons, the same statistics are needed for each base and as the production rate changes, longer measurement time is needed for lower power levels. At 6.4 Watts 506.96 and for 3.7 Watts 336.11 events of concurrent 6 photon detections were collected. This corresponds to a count rate of $13.11\frac{1}{\text{min}}$ compared to $2.31\frac{1}{\text{min}}$.

Figure 6.2 shows counts (normalized by the total number of counts) for local measurements in the Z and X basis on each qubit in comparison to expected values for a noisy state according to 5.6 where the p parameter is again taken from the following noise analysis in chapter 6.4. Count patterns for a $X^{\otimes 6}$ and $Y^{\otimes 6}$ measurement are equal and have only 2 large entries for $H^{\otimes 6}$ and $V^{\otimes 6}$ (around 0.3). The remaining ones are in the order of 0.01. Figure 6.2b shows that the recorded values are in good agreement within the errorbars. Measurements in $Z^{\otimes 6}$ for 6.4 Watt are shown in figure 6.2a, also with minimal discrepancies to theoretical values.

Such graphs can be plotted for all of the measured base configurations, but the only values that are used to calculate the density matrix entries are of the form $\langle\left(X^{\otimes k} \otimes Y^{\otimes l} \otimes Z^{\otimes m} \otimes \mathbb{1}^n\right)\rangle$ (see eq. 3.7). They are calculated from the counts in all bases and can therefore bee seen as a distillate of the measurement. These 83 values are shown in figure 6.3. On the x axis, all possible combinations where $k+l+m+n=N$ holds are listed, not respecting any order. Blue points indicate the measured data, including errors. Red points represent an ideal, but mixed $\mathcal{D}_6^3$ state (according to the noise model). Yellow points are calculated

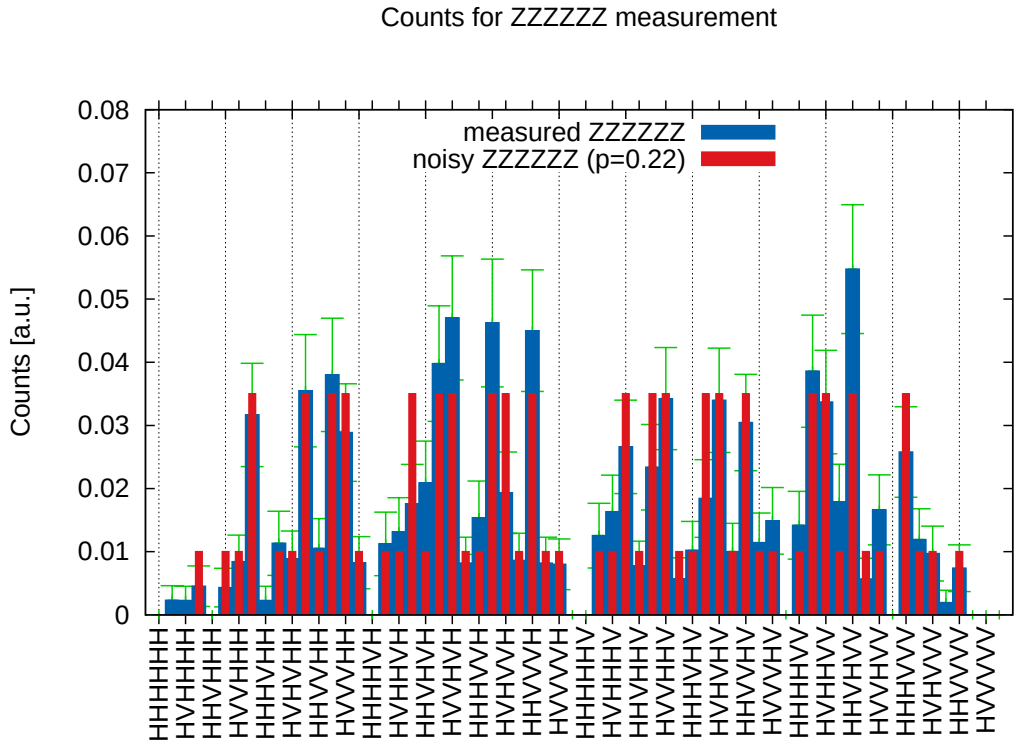

(a) Measurement at 6.4 Watt

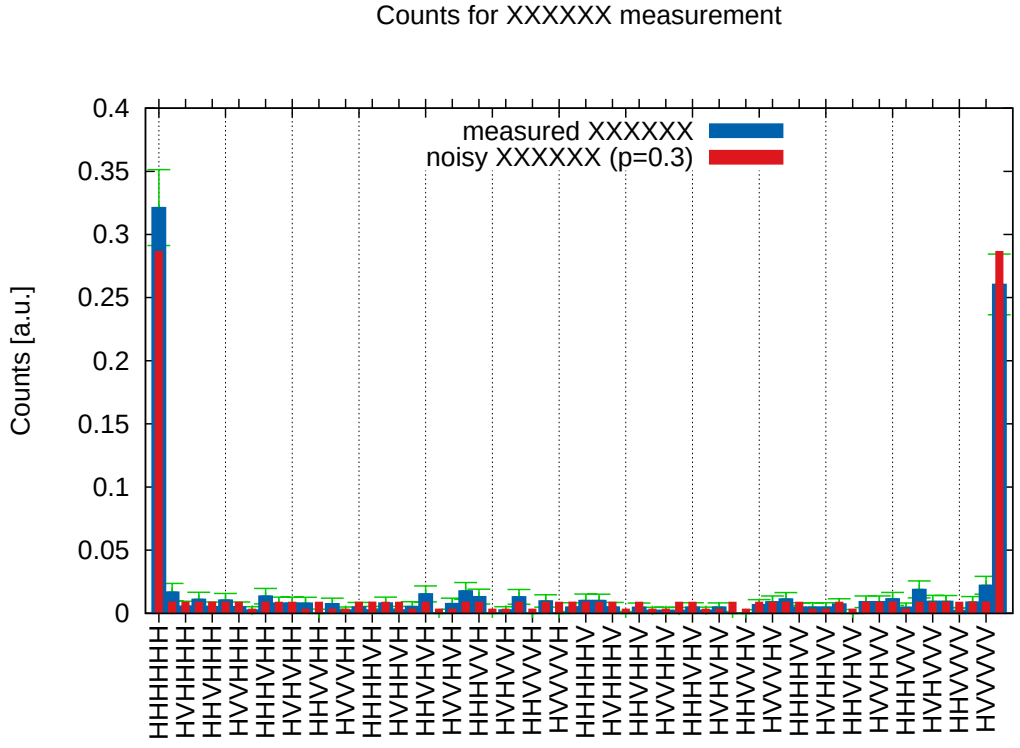

(b) Measurement at 3.7 Watt

Figure 6.2: Counts of a ZZZZZZ basis measurement (blue) compared to expected values (red) for a noisy Dicke state

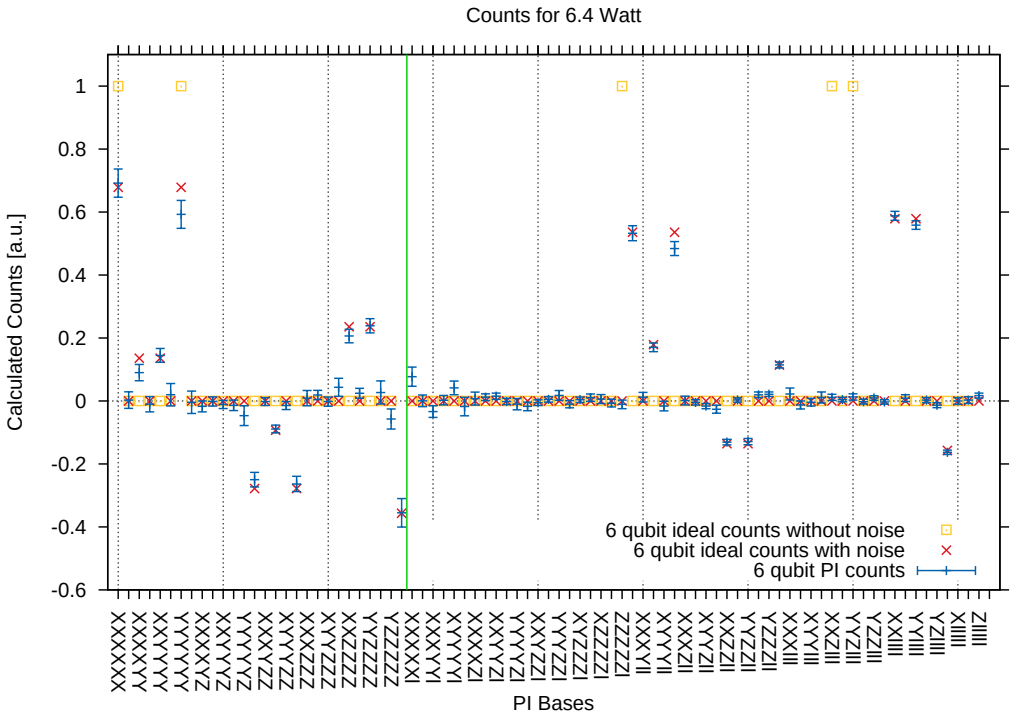

Figure 6.3: PI correlations for the 6.4 Watt measurement in comparison to the expected ideal and ideal noisy ($p = 0.3$) $\mathcal{D}_6^3$ state are plotted. The green vertical line marks the first occurrence of a correlation involving $\mathbb{1}$.

from an ideal $\mathcal{D}_6^3$ state. Because measured data lie closest to expected values for a noisy state, a mixture rather than a pure state is measured. The green vertical line marks the position where $\mathbb{1}$ measurements appear for the first time. For increasing numbers of such projections, the error is reduced, because the values are gained by averaging more and more measured counts.

The density operator ρ itself is best visualized in a 3 dimensional bar graph. In Figure 6.4 it is plotted for the 6.4 Watt measurement, using directly the measured counts (6.4a and 6.4b) as well as feeding the data through the maximum likelihood algorithm (6.4c and 6.4d). For comparison, an ideal and ideal noisy $\mathcal{D}_6^3$ state is plotted in the same way in appendix F. The typical plateau, that emerges for noisy states around the central block, is visible in the measured data. As described in chapter 5.4, the average height of these parts will later be used to estimate the noise level.

The directly reconstructed density matrix shows unusual high values in entries on the very border. This fence like structure is visible in the real and imaginary part. It can be explained by the amount of data points that contribute to individual density matrix

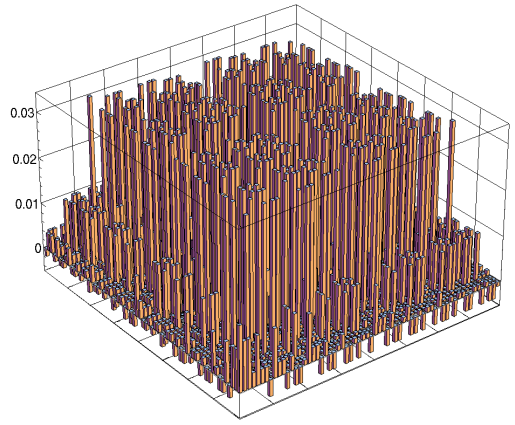

(a) Real part of measured and unmodified data in density matrix form

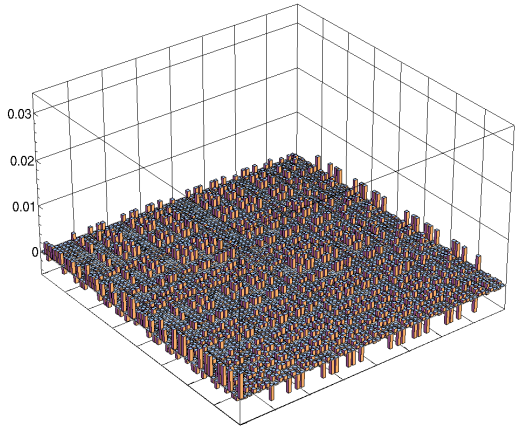

(b) Raw imaginary part

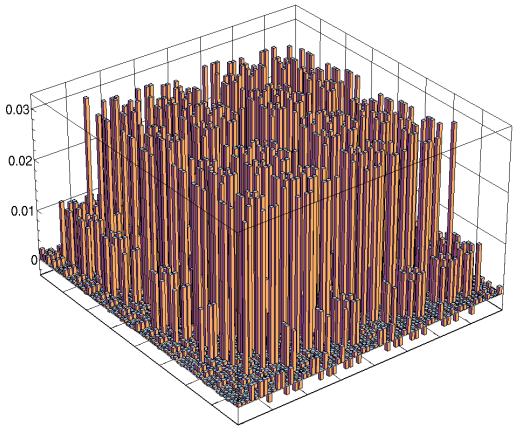

(c) Real part of MLE optimized density matrix

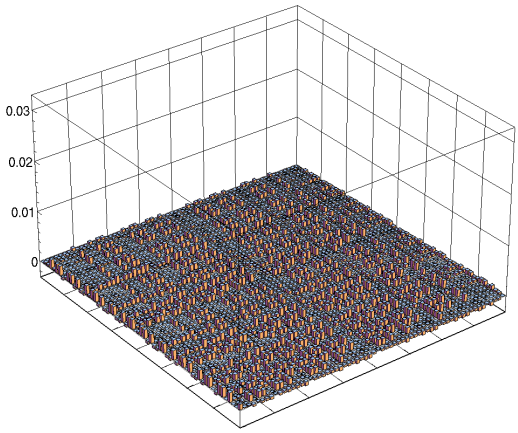

(d) Imaginary part of MLE optimized density matrix

Figure 6.4: 3 dimensional bar plot of the density matrix for a 6 qubit tomography at 6.4 Watt.

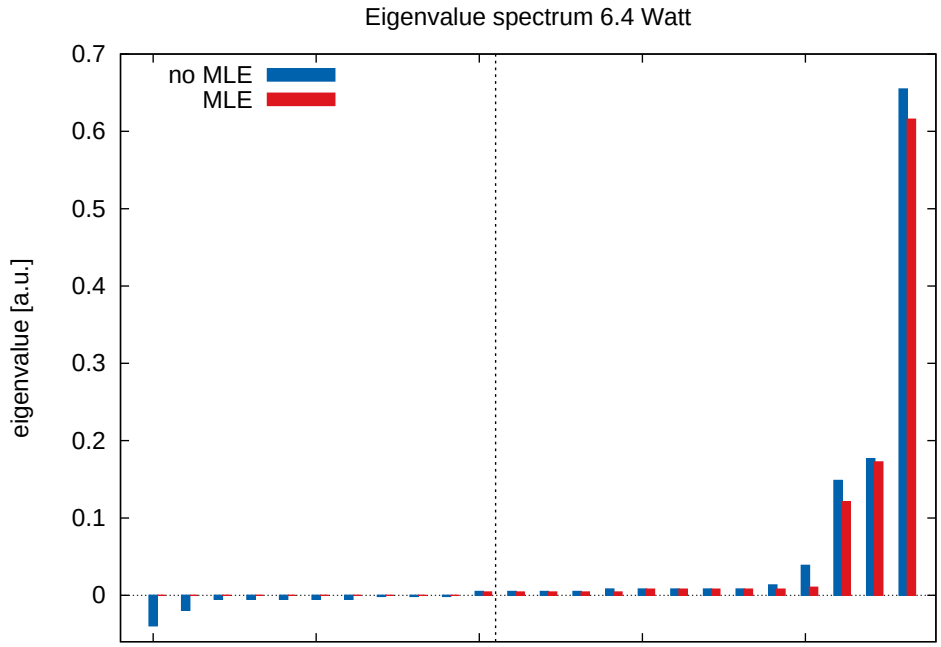

Figure 6.5: Partial eigenvalue spectrum of a reconstructed density matrix before (blue) and after (red) the MLE optimization for a measurement at 6.4 Watt. Eigenvalues are ordered by magnitude; at the vertical dotted line values are left out.

entries. In appendix B the number of values that are used in the PI reconstruction formula on each entry in ρ are shown as a color plot. On the border, 3 times more values are added or subtracted resulting in the final value. Because errors sum up in this operations, they are expected to be larger there, compared to other entries. The optimized density operator in figures 6.4c and 6.4d shows significantly less of these entries. Overall 2 main differences are visible:

- The average contribution of the imaginary part is reduced
- The artifacts on the border entries are nearly completely erased

These 2 points show the power of the used MLE approach. Both features that were suppressed are not part of the ideal state. Another feature should be the push towards a physical state. This can be seen on the eigenvalue spectrum. An ideal $\mathcal{D}_6^3$ state has a single eigenvalue that is 1, all other 63 are equal to zero. Its noisy version has one large one (value dependent on the noise parameter p) and 2 smaller ones, the rest is also zero. Negative eigenvalues are forbidden, because the are probability to detect the system in their eigenvector. Figure 6.5 shows the (partial) eigenvalue spectrum of the 6.4 Watt measurement before and after MLE optimization. The eigenvalues are ordered by magnitude. The interesting areas are around the largest and smallest values. At the dotted vertical line, 40 values are left out to shrink the graphs size. The blue bars, not

optimized via MLE, show several negative eigenvalues, so the matrix directly recovered from the measured data cannot be considered a physical density matrix. If it is optimized (red bars), the negative eigenvalues vanish. Also the 3rd, 4th etc. largest eigenvalues shrink. The resemblance to an ideal $\mathcal{D}_6^3$ state is increased. To quantify the distance, the fidelity measure is used.

6.3 Fidelity

The standard measure to judge the quality of a measured state to its theoretical version is the fidelity (see chapter 2.1.4). For the 2 mentioned measurements at 3.7 and 6.4 Watt, with or without use of MLE, the following fidelities were reached:

		raw measured		**optimized MLE**	
		3.7 **Watt**	6.4 **Watt**	3.7 **Watt**	6.4 **Watt**
fidelity	$\mathcal{D}_6^3$	0.6775	0.6305	0.6257	0.6129
	$(\mathcal{D}_6^3)_{\mathrm{n}}$	0.9625	0.9693	0.8757	0.9023

$(\mathcal{D}_6^3)_{\mathrm{n}}$ denotes the noisy state defined via eq 5.6. As expected, comparison to the state without the noise model yields to low values whereas including the noise model pushes the fidelity to 96%. Astonishing is the decrease for the matrices that were optimized using the MLE method. A drop of about 7% is very large. If the optimized density matrix is used to calculate expected counts in $X^{\otimes 6}$, $Y^{\otimes 6}$ and $Z^{\otimes 6}$ to calculate the overlap with the symmetric space of $\mathcal{D}_6^3$ again, ≈4% are lost for the 6.4 Watt measurement and ≈10% for the 3.7 Watt one.

Judging from these values, MLE optimization seems to increase the distance to the ideal state. On the other side is it necessary to create a valid density matrix. Unfortunately, it is not possible to pinpoint the exact reason for the decrease. One possibility is that the algorithm does not reach its global optimum. In this case a state that is more distant would be recovered. However this would be an artifact of the used optimization routine[1] and can be excluded with more elaborate versions. One example would be convex optimization, where the global optimum is always reached[6, 33].

Overall the fidelities show that the described setup allows efficient creation and detection of the desired state. In the previous sections, estimated noise parameters were already used. In the following section, the needed values are finally calculated.

6.4 Noise analysis

The plateau like structures in the previous plots are the indicator for the presence of noise. Figure 5.6 in chapter 5.4 identifies entries in the density operator with states that are

[1] in this case the standard fminunc function of MATLAB

	3.7Watt		6.4Watt	
	no MLE	**MLE**	**no MLE**	**MLE**
$\mathcal{D}_6^2$	0.2570	0.3053	0.1959	0.2231
$\mathcal{D}_6^3$	0.2475	0.1267	0.1840	0.0967
$\mathcal{D}_6^4$	0.3972	0.5112	0.3028	0.4093
average	0.3005	0.3144	0.2275	0.2430

Table 6.1: Noise parameter p from eq. 5.6 for different pump powers calculated from different parts of the density operator. The results are compared to the direct result form eq. 3.2 and the MLE algorithm as well as a convex optimization algorithm.

crated through higher order noise. To estimate the noise parameter p , the average values for the different noise parts are needed. Once they are known, equation 5.8 for $\mathcal{D}_6^4$ and the analogue versions for $\mathcal{D}_6^2$ and $\mathcal{D}_6^3$ are used.

Table 6.1 lists the calculated values for the optimized and not optimized density matrix. Compared to the change in fidelity, the change in average p is very small. Individual estimations however show large changes. The noise model assumes that $\mathcal{D}_6^4$ and $\mathcal{D}_6^2$ originate from the creation of 8 entangled photons in the crystal. Therefore lower contributions are expected for lower pump powers. Indeed estimates for p reduce with the power in the cavity.

In the default base pattern (see eq. 2.1) each state consists of multiple components in the density operator. Without any knowledge of the ideal version, an identification is difficult. The choice of basis is build in the reconstruction formulae 3.2 and 3.7, but can be changed at a later time. 2 quantities can describe the states that are produced by the SPDC source and the linear setup: the number of qubits and the number of excited qubits. A change to a basis set that incorporates these values, rather than polarization, will greatly simplify the pattern of the density operator. Such change of bases is well known from spin-$\frac{1}{2}$ systems. Instead of describing the state in terms of individual quantum numbers like $|j_1, j_2; m_1, m_2\rangle$($j_i$ is the angular momentum quantum number and $m = -j, -j+1, ..., j$), values describing the total system are used: $|j = j_1 + j_2; m = m_1 + m_2\rangle$. For spin, the 4 possible configurations $|\uparrow\uparrow\rangle$, $|\downarrow\uparrow\rangle$, $|\uparrow\downarrow\rangle$ and $|\downarrow\downarrow\rangle$ are now described by the triplet $|s = 1, m = \pm 1, 0\rangle$ and singlet $|s = 0, m = 0\rangle$ state.

$$|1,1\rangle = |\uparrow\uparrow\rangle; \quad |1,0\rangle = \tfrac{1}{\sqrt{2}}\left(|\uparrow\downarrow\rangle + |\downarrow\uparrow\rangle\right); \quad |1,-1\rangle = |\downarrow\downarrow\rangle$$
$$|0,0\rangle = \tfrac{1}{\sqrt{2}}\left(|\uparrow\downarrow\rangle - |\downarrow\uparrow\rangle\right)$$

If these vectors are used as base vectors and the system is e.g. in a triplet state, the nonzero entries reduce from 4 to 1, directly marking the triplet state the system is in. In addition the matrix becomes block diagonal, so only of the size $2j + 1$, with $j = \frac{N}{2}$, for each group of j are nonzero. In the above example, the first ($j = 1$) block is 3x3 elements, the second

($j = 0$) 1x1 element large. The term block refers to the group of new base vectors with the same j. Therefore the blocks are often named after this number. To obtain the new vectors, different approaches are possible. The standard one in textbooks uses the Clebsch Gordon coefficients[34]. Here, a more specific, but easier formula is used.

In case of the symmetric Dicke State, the first block ($j = 3$) will have the base vectors

$$\begin{array}{c} \\ |\mathcal{D}_6^0\rangle \\ |\mathcal{D}_6^1\rangle \\ |\mathcal{D}_6^2\rangle \\ \vdots \\ |\mathcal{D}_6^6\rangle \end{array} \begin{array}{c} \begin{array}{ccccc} \langle\mathcal{D}_6^0| & \langle\mathcal{D}_6^1| & \langle\mathcal{D}_6^2| & \cdots & \langle\mathcal{D}_6^6| \end{array} \\ \begin{bmatrix} \mathrm{x} & \cdots & & & \\ \vdots & \ddots & & & \\ \vdots & & & & \\ \vdots & & & & \\ \vdots & & & & \end{bmatrix} \end{array} \tag{6.1}$$

The density matrix will be cast in the from

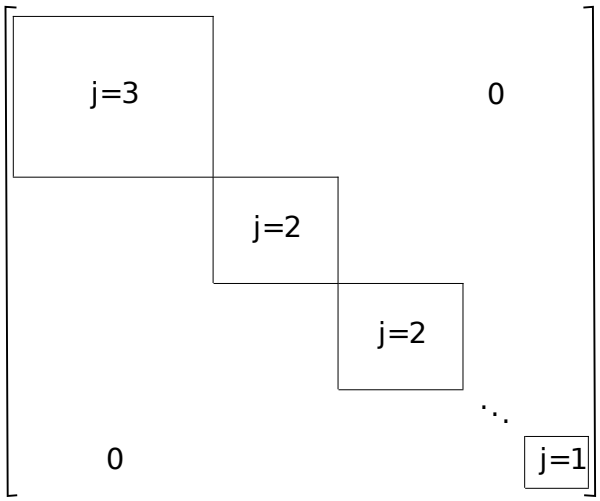

The structure 6.1 forms the $j = 3$ block. In case of a PI symmetric state, all blocks with equal j will be degenerate. An easy formula for the new base vectors is given in[10]:

$$|B_{j,m}\rangle = |\mathcal{D}_{2j}^{m+j}\rangle \otimes |\Psi^-\rangle^{\frac{N}{2}-j}$$

with the Bell State $|\Psi^-\rangle = \frac{1}{\sqrt{2}}(|01\rangle - |10\rangle)$ and the symmetric Dicke state $|\mathcal{D}\rangle$. m varies from 0 to $2j$: from 0 to the number of base vectors in the corresponding block. So $|B_{3,6}\rangle$ to $|B_{3,0}\rangle$ are the wanted vectors for $j = 3$. The recreation of the set in 6.1 is immediately visible. For $j = 3$, the exponent on $|\Psi^-\rangle$ is zero and the Dicke states with different numbers of excited qubits form the new base vectors is left.

Figure 6.6 shows the 3 non-degenerate blocks for the 6.4 Watt measurement. The imaginary part has no significant contributions and is therefore hidden. All values in the $j = 2$ and $j = 1$ parts are below 10^{-3} and 10^{-4}, so there are no significant entries either.

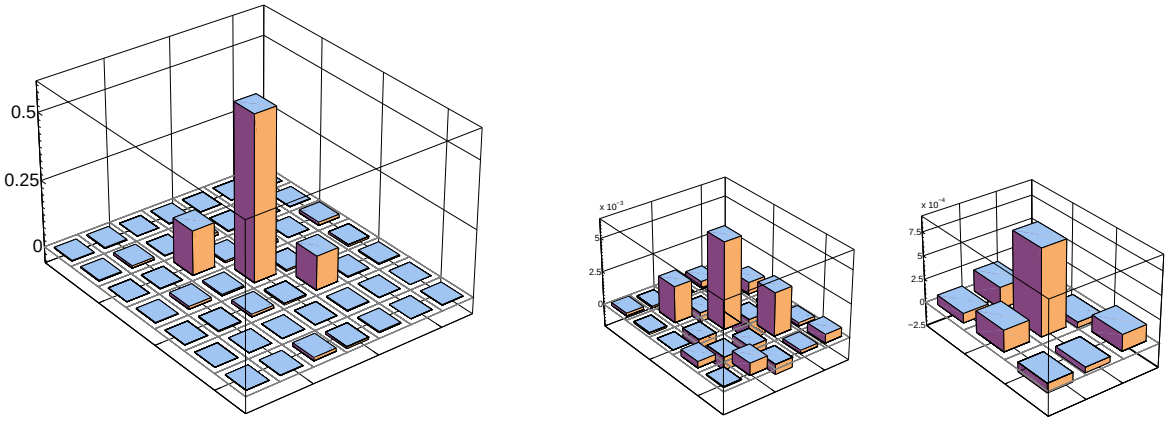

(a) $j = 3$ part (b) $j = 2$ part (c) $j = 1$ part

Figure 6.6: Real part of nonzero blocks on the diagonal of the matrix from 6.4. Contributions from b) and c) are neglectable. The 3 significant parts in a) correspond to $\mathcal{D}_6^2$, $\mathcal{D}_6^3$ and $\mathcal{D}_6^4$ (left to right)

Figure 6.6a shows 3 bars that represent $\mathcal{D}_6^2$, $\mathcal{D}_6^3$ and $\mathcal{D}_6^4$. Unfortunately it is not possible to extract p directly from this representation, because the noise model formula relies on the $|\mathrm{H}\rangle|\mathrm{V}\rangle$ basis. Apart from making contributing state easier to identify, the amount of values that are needed to classify the state uniquely are reduced dramatically. Instead of a full 64x64 matrix (4096 entries) 3 smaller matrices with 83 entries in total are sufficient. Like the tomographic scheme, the symmetry in the state is used to make things easier.

7 Alignment Errors

Qubits in this experiment are polarization coded. Thus, reliability of taken data depends heavily on proper alignment of the analysis part. All used components should perform the same operations for equal base configurations. However imperfections in the waveplates itself and alignment errors can distort results. For example if just a beam of horizontal photons is fed into the system, all arms should register the photons as horizontal polarized. Discrepancies will show up if individual arms have offsets in their waveplate alignment. Instead of projecting onto the proper axis, a different one is created through the alignment errors. The reconstruction equations (3.7 and 3.2) always assume perfect measurements in the required base configuration, so the error will effect the measured state.

The following chapter investigates the effect of alignment errors in a 2 photon setup, designed to perform tomography on the Bell State $|\Phi^+\rangle$. An estimate is given how severe the impact will be on the result and if reconstruction of the offsets is possible. The choice was made because this system seems manageable in its size and all alignment, data acquisition and data processing is the same in the 6 photon setup. Results can be transferred to the bigger setup. The alignment process is carried out with a (horizontal) polarizer placed in an arm and with just the HWP in place. Rotation of the wave plate leads to sinusoidal signals in the in the 2 output channels of the PBS, phase shifted by π. A fitting routine determines the maximum and outputs the offset from the actual 0° position. This is repeated several times until the angles, that need to be corrected are below $\approx 0.05°$. This value is found to be within the uncertainties resulting from noise in the detectors. This is repeated in each arm separately and with a plus polarizer for the quarter wave plate. The latter one shows larger fluctuations from iteration to iteration. Tests in the 3 standard bases show that the overall error is maximally $\approx 7‰$; this is the percentage of photons that will be guided in the wrong channel. Errors from the PBS themselves are in the order $\approx$ 1-2‰. In principle, this alignment method should be quite reliable. Increasing alignment errors during longer measurement times are possible, when the motors controlling the wave plates, are producing an offset over time.

Any alignment error should manifest itself directly in the recorded counts. In the following part, simulations with the $\mathcal{D}_2^1$ (also known as $|\Psi^+\rangle$) state are investigated. Simulated measurement data are generated by taking the ideal density matrix ρ_{ideal} and calculating the expected counts for each base and polarization combination. For 2 qubits, there are 9 unique base combinations, each leading to 4 count rates, originating from HH, HV, VH or

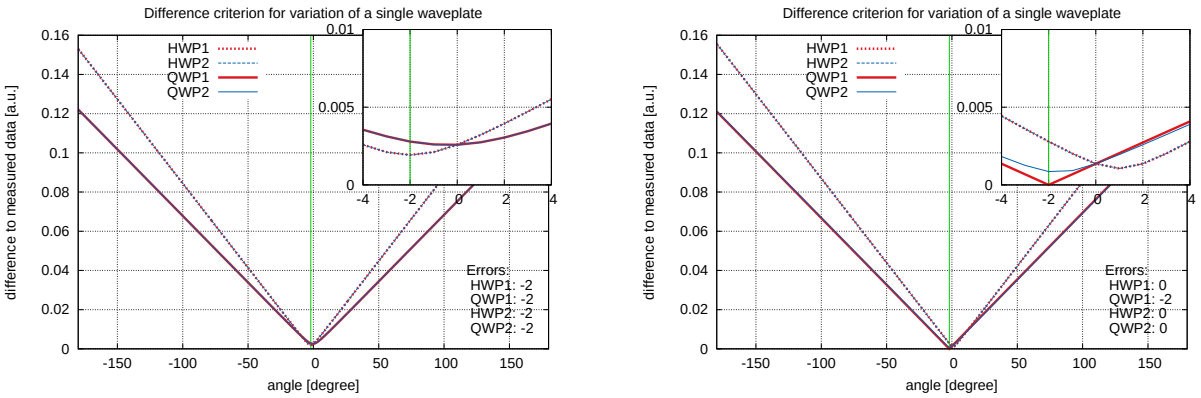

(a) offset angles of -2° on all 4 waveplates

(b) offset angle of -2° only on the QWP on qubit 1

Figure 7.1: Size of difference vector between simulated counts for a given offset set and counts just on one waveplate. The HWP's are dotted, qubits are color coded.

VV events, so in total there are 36 values recovered. Instead of using the ideal (eq. 2.4) projector, another measurement base is created via 2.7 for a given set of offset angles on each of the 4 wave plates. These offsets are written in a shorter matrix form:

$$\begin{array}{c} \\ \text{Qubit 1} \\ \text{Qubit 2} \end{array} \begin{array}{c} \begin{array}{cc} \text{HWP} & \text{QWP} \end{array} \\ \begin{bmatrix} \text{offset angle}[^\circ] & \text{offset angle}[^\circ] \\ \text{offset angle}[^\circ] & \text{offset angle}[^\circ] \end{bmatrix} \end{array} \tag{7.1}$$

In addition, these counts are disturbed via a Poissonian distribution to simulate generic noise of the setup. In the end, there is 2 times a set of 36 counts, representing the measured and artificially ill aligned data. Values of the latter one depend on the 4 offset angles of the wave plate. To find these angles, the 36 counts written as a vector (see appendix C for example values). These two vectors, $\vec{c}_{\text{measured}}$ and $\vec{c}_{\text{calculated}}$, are subtracted the size of the resulting vector $\vec{d} = |\vec{c}_{\text{measured}} - \vec{c}_{\text{calculated}}|$is minimized:

$$\min\left(\left|\vec{d}\right|\right) = \min\left(|\vec{c}_{\text{calculated}} - \vec{c}_{\text{measured}}|\right)$$

This length is a function of the 4 offset angles and should be minimal if the set of offset angles matches the ones in the setup producing the measured data.

To test, if this function indeed will find a minimum, different combinations of offsets were tested. Figure 7.1 contains 2 graphs, showing results for an offset of -2° on all 4 waveplates (7.1a) and just on the quarter wave plate for qubit 1 (7.1b). The angle of -2° is an arbitrary choice here. The y axis shows the length of $\vec{d}$, the x axis the artificial offset of *a single wave plate* where type and qubit are color and line style coded. The choice to only alter the offset of a single wave plate at a time was made to keep the graph clear, as variation of 2 plates at the same time could only be visualized in a 3D graph and more would not be possible. Both figures show that minima are reached if the wave plate with

the artificial offset hits the used value. 7.1b shows the minimum to be equal to zero, but this is expected because QWP #1 is the only one, which had an offset imposed. Figure 7.1a shows that the length decreases, if assumed angles approach the used offset. Both graphs have a global minimum. The same calculation was performed for all possible combinations of an -2° offset on the 4 possible positions. The results shows 2 important points:

- if either one or both HWP's have an offset, both HWP have a minimum at the correct position if both QWP's have the same offset.
- offsets for the QWP's are correctly found if no offsets are on the HWP's or both HWP's have the same offset

Again all graphs show a global minimum. A test of the algorithm with all possible combinations of -2° offset and no artificial noise on the counts yields:

applied [°]	**reconstructed [°]**
$\begin{bmatrix} 0 & 0 \\ 0 & 0 \end{bmatrix}$	$\begin{bmatrix} 0 & 0 \\ 0 & 0 \end{bmatrix}$
$\begin{bmatrix} -2 & 0 \\ 0 & 0 \end{bmatrix}$	$\begin{bmatrix} -2.91 & 0.00 \\ 0.91 & 0.00 \end{bmatrix}$
$\begin{bmatrix} 0 & 0 \\ -2 & 0 \end{bmatrix}$	$\begin{bmatrix} -2.91 & 0.00 \\ 0.91 & 0.00 \end{bmatrix}$
$\begin{bmatrix} 0 & -2 \\ 0 & 0 \end{bmatrix}$	$\begin{bmatrix} 0.78 & -1.99 \\ -0.78 & -0.01 \end{bmatrix}$
$\begin{bmatrix} 0 & 0 \\ 0 & -2 \end{bmatrix}$	$\begin{bmatrix} -0.78 & -0.001 \\ 0.78 & -1.99 \end{bmatrix}$
$\begin{bmatrix} -2 & 0 \\ -2 & 0 \end{bmatrix}$	$\begin{bmatrix} -2.25 & 0.00 \\ -1.75 & 0.00 \end{bmatrix}$
$\begin{bmatrix} -2 & -2 \\ 0 & 0 \end{bmatrix}$	$\begin{bmatrix} -1.90 & -2.00 \\ -0.09 & 0.00 \end{bmatrix}$
$\begin{bmatrix} -2 & 0 \\ 0 & -2 \end{bmatrix}$	$\begin{bmatrix} -0.09 & 0,00 \\ -1.90 & -2.00 \end{bmatrix}$

applied [°]	**reconstructed [°]**
$\begin{bmatrix} 0 & -2 \\ -2 & 0 \end{bmatrix}$	$\begin{bmatrix} -1.90 & -2.00 \\ -0.09 & 0.00 \end{bmatrix}$
$\begin{bmatrix} 0 & 0 \\ -2 & -2 \end{bmatrix}$	$\begin{bmatrix} -0.09 & 0.00 \\ -1.90 & -2.00 \end{bmatrix}$
$\begin{bmatrix} 0 & -2 \\ 0 & -2 \end{bmatrix}$	$\begin{bmatrix} 0.99 & -2.00 \\ -1.00 & -2.00 \end{bmatrix}$
$\begin{bmatrix} -2 & -2 \\ -2 & 0 \end{bmatrix}$	$\begin{bmatrix} -3.83 & -1.99 \\ -0.165 & -0.00 \end{bmatrix}$
$\begin{bmatrix} -2 & 0 \\ -2 & -2 \end{bmatrix}$	$\begin{bmatrix} -0.16 & 0.00 \\ -3.83 & -1.99 \end{bmatrix}$
$\begin{bmatrix} -2 & -2 \\ 0 & -2 \end{bmatrix}$	$\begin{bmatrix} -7.10 & -1.99 \\ 5.10 & -2.00 \end{bmatrix}$
$\begin{bmatrix} 0 & -2 \\ -2 & -2 \end{bmatrix}$	$\begin{bmatrix} -7.10 & -2.00 \\ 5.10 & -1.99 \end{bmatrix}$
$\begin{bmatrix} -2 & -2 \\ -2 & -2 \end{bmatrix}$	$\begin{bmatrix} -2.61 & -1.99 \\ -1.38 & -2.00 \end{bmatrix}$

Again 2 points are important:

- Offsets on the QWP are found correctly in any combination
- The offset of the HWP are only correct in sum

The last point can be seen on the results from $\begin{bmatrix} 0 & -2 \\ 0 & 0 \end{bmatrix}$. The overall offset on the HWP is zero, but 0.78° and -0.78° are found. Although the individual values are not correct, the

sum is. Adding up the used offsets gives zero, as well as adding up the recovered angles. All investigated combinations show this effect. Later, this behaviour is found to be a feature of the states symmetry.

To check performance under more experimental like conditions, noise id added to the simulated counts. In this configuration, the simulated data, that represent measured ones, are generated and Poissonian noise is applied. These steps are repeated 500 times for each combination, leading to histograms of reconstructed angles. Results suggest that an extraction of any deadjustment on the QWP's should be possible, whereas the HWP's only reveal the overall offset. For the latter, the sum of the reconstructed offsets always fits the sum of the used offsets. Investigating more experiment like behaviour, poissonian noise was added to the calculated correlations and the reconstruction performed 500 times for each offset combination. Figure 7.2 shows 2 examples. In the upper left corner the used offset configuration, used to simulate the setup, is shown. Found angles are plotted as histograms with the qubits color and the waveplate type line style coded. The previous results show that, at least for the HWP's, the sum of the reconstructed angles might be of interest, which is plotted as a yellow bars. To mark the average of he found angles, vertical lines with the same colour and pattern are printed. From the graphs (including the ones not shown) the following observations are done:

- The averages of the recovered offsets show acceptable agreement for the individual QWP's, but not for HWP's.
- The sums reflect the overall offset correctly. For the QWP's, this is a consequence from the previous point, but not for the HWP's.
- The shape of the histogram for the angles of HWP1 and HWP2 is symmetric by an axis between. This pattern can be explained because the sum of the found angles of HWP1 and HWP2 recreate the sum of the used offsets for these waveplates. This leads to symmetric patterns.
- Scattering is below 0.1° in each direction for the correctly recovered offsets with the assumed Poissonian noise.

This shows that there is no significant performance change is visible when statistics are added. Before testing the performance on actual data, the behaviour or the $|\Phi^+\rangle$ state for certain combinations of offsets will be investigated.

7.1 Symmetry of $|\Phi^+\rangle$

The results suggest a systematic ambiguity, at least for the HWP's. An operator describing the offset rotation of the waveplates and therefore simulating the offset would read

$$\mathcal{O}(\alpha, \beta) = (\mathrm{HWP}(\alpha) \otimes \mathbb{1})(\mathbb{1} \otimes \mathrm{HWP}(\beta)) \tag{7.2}$$

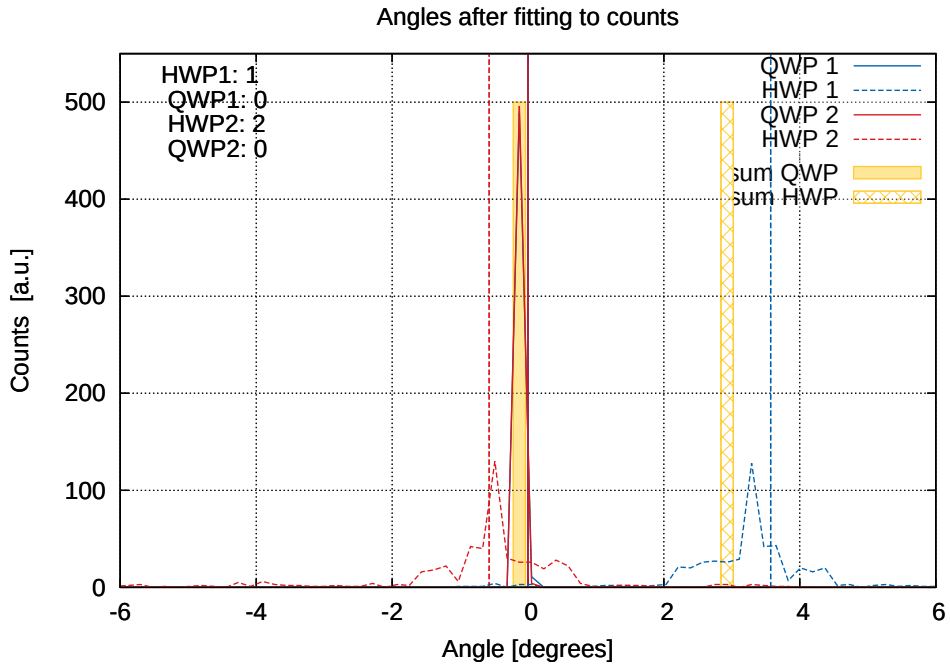

(a) Offset +1° on HWP1 and +2° on HWP2

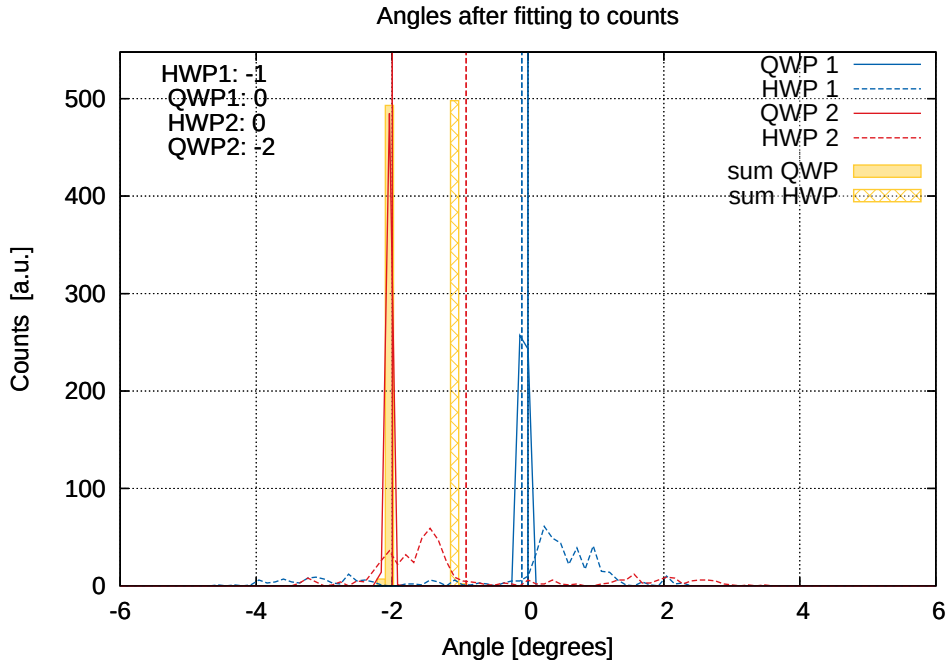

(b) Offset +2° on QWP1 and -2° on HWP2

Figure 7.2: Reconstructed angle offsets for 500 iterations with noise on the simulated counts. More plots with different angle configurations can be found in appendix E

for an offset just on both HWP's, misaligned by the angles α and β. The effect on a density operator ρ can be evaluated via

$$\mathcal{O}(\alpha,\beta)\ \rho\,\mathcal{O}^{\dagger}(\alpha,\beta)$$

Because the operator is unitary ($\mathcal{O}\mathcal{O}^{\dagger} = \mathbb{1}$), a commutation with ρ ($[\mathcal{O},\rho] = 0$) would cancel out the effect. In the case of the $\mathcal{D}_2^1$ state, this is true for any offset of the type

$$\begin{bmatrix} -\alpha & 0 \\ \alpha & 0 \end{bmatrix}$$

where α can be any positive or negative angle. This effect is lost for symmetric Dicke states with more qubits but is a feature of the Bell States for different combinations. Derivations for the above relation and results for the Bell States are shown in D. If such a symmetry is present by chance, the offsets will not be detectable. In addition, the reconstruction will see the above symmetry as a valid result and is likely to produce arbitrary offsets on the HWP's. However, this changes dependent on the state that is analyzed.

7.2 Reconstructed offsets for measured data

A full tomographic of the Bell State $|\Phi^+\rangle = \frac{1}{\sqrt{2}}(|\mathrm{HH}\rangle + |\mathrm{VV}\rangle)$ was measured by Philipp Kurpiers (Bachelor student) with artificial offsets on certain wave plates. Table 7.1 shows reconstructed angles for the HWP's and QWP's. Both measurements were calibrated independently, so any value should be considered with respect to the $\begin{bmatrix} 0 & 0 \\ 0 & 0 \end{bmatrix}$ outcome in the corresponding table, which might reflect an overall deadjustment. The Φ^+ state is invariant for any equal offset on both HWP's (see appendix D), what can be seen on the results when both have zero offset applied (right table). Reconstructed values are similar, but can have quite different absolute values.

On the left side, only the HWP's are changed. The simulation findings, that sum does reproduce the applied offset is not visible here. Despite that the sign is not recovered correctly, the absolute value seems to vary randomly and not only because of the afore mentioned symmetry. Angles for the QWP's are constant and can be considered to have physical meaning here.

The right table contains only variations of the QWP's. Taking the applied zero setting on all waveplates as a reference, the values do match the applied offsets within $\pm 0.5°$. Angles for HWP's however have no clear connection expected values, but are within the same order of magnitude. This random behaviour was expected from the simulations.

In section C measured and theoretical values of the correlation vector are shown to illustrate the behaviour of the optimization criterion for data from an experiment. Measured and reconstructed are very similar, but not in all regions of the vector. For example the HH correlation in the XX base is recovered perfectly whereas the HV and VH correlations in the ZZ base have big discrepancies. The columns "calculated" and "ideal" show values for

applied [°]	recovered [°]	applied [°]	recovered [°]
$\begin{bmatrix} -2 & 0 \\ 0 & 0 \end{bmatrix}$	$\begin{bmatrix} 2.16 & -3.20 \\ -0.17 & -4.37 \end{bmatrix}$	$\begin{bmatrix} 0 & -2 \\ 0 & 0 \end{bmatrix}$	$\begin{bmatrix} 0.09 & -4.02 \\ 0.98 & -2.11 \end{bmatrix}$
$\begin{bmatrix} -1 & 0 \\ 0 & 0 \end{bmatrix}$	$\begin{bmatrix} 2.03 & -3.82 \\ 0.07 & -4.93 \end{bmatrix}$	$\begin{bmatrix} 0 & -1 \\ 0 & 0 \end{bmatrix}$	$\begin{bmatrix} 2.58 & -3.19 \\ 3.49 & -2.53 \end{bmatrix}$
$\begin{bmatrix} 0 & 0 \\ 0 & 0 \end{bmatrix}$	$\begin{bmatrix} 0.61 & -3.01 \\ 0.49 & -4.14 \end{bmatrix}$	$\begin{bmatrix} 0 & 0 \\ 0 & 0 \end{bmatrix}$	$\begin{bmatrix} 0.18 & -1.84 \\ 1.33 & -2.06 \end{bmatrix}$
$\begin{bmatrix} 1 & 0 \\ 0 & 0 \end{bmatrix}$	$\begin{bmatrix} 1.8 & -3.50 \\ 1.63 & -4.59 \end{bmatrix}$	$\begin{bmatrix} 0 & 1 \\ 0 & 0 \end{bmatrix}$	$\begin{bmatrix} -0.46 & -1.43 \\ 0.39 & -2.69 \end{bmatrix}$
$\begin{bmatrix} 2 & 0 \\ 0 & 0 \end{bmatrix}$	$\begin{bmatrix} 0.12 & -3.95 \\ 1.12 & -5.20 \end{bmatrix}$	$\begin{bmatrix} 0 & 2 \\ 0 & 0 \end{bmatrix}$	$\begin{bmatrix} 4.30 & -0.34 \\ 4.98 & -2.52 \end{bmatrix}$
$\begin{bmatrix} 0 & 0 \\ -2 & 0 \end{bmatrix}$	$\begin{bmatrix} 3.79 & -3.91 \\ 4.76 & -5.13 \end{bmatrix}$	$\begin{bmatrix} 0 & 0 \\ 0 & -2 \end{bmatrix}$	$\begin{bmatrix} 1.144 & -1.90 \\ 2.60 & -4.09 \end{bmatrix}$
$\begin{bmatrix} 0 & 0 \\ -1 & 0 \end{bmatrix}$	$\begin{bmatrix} 2.39 & -3.07 \\ 2.96 & -4.46 \end{bmatrix}$	$\begin{bmatrix} 0 & 0 \\ 0 & -1 \end{bmatrix}$	$\begin{bmatrix} 3.44 & -2.13 \\ 4.57 & -3.30 \end{bmatrix}$
$\begin{bmatrix} 0 & 0 \\ 1 & 0 \end{bmatrix}$	$\begin{bmatrix} 1.57 & -4.02 \\ -0.34 & -5.12 \end{bmatrix}$	$\begin{bmatrix} 0 & 0 \\ 0 & 1 \end{bmatrix}$	$\begin{bmatrix} 0.57 & -2.29 \\ 1.57 & -1.60 \end{bmatrix}$
$\begin{bmatrix} 0 & 0 \\ 2 & 0 \end{bmatrix}$	$\begin{bmatrix} 3.50 & -3.06 \\ 1.46 & -4.17 \end{bmatrix}$	$\begin{bmatrix} 0 & 0 \\ 0 & 2 \end{bmatrix}$	$\begin{bmatrix} -0.19 & -1.89 \\ 0.69 & -0.24 \end{bmatrix}$

Table 7.1: Recovered data from an artificially deadjusted tomography of the Φ^+ state.

the ideal offset just on a single waveplate and of the ideal state without any perturbation. In comparison, only a few entries differ, the majority is the same. This is expected, because an offset on any HWP will just alter any results measured in the X basis. This feature could be exploited in a different optimization result where only parts of the correlation vector are investigated that actually would change for the considered waveplates.

7.3 Effects on Eigenvalues and Fidelity

Offsets on different waveplates lead to different behaviour of the eigenvalues and fidelities. The smallest eigenvalue (-0.0726) was found for the combination $\begin{bmatrix} 0 & -2 \\ 0 & -2 \end{bmatrix}$. The numeric value depends on the value (it will increase for bigger offsets) but this pattern immediately produces large negative eigenvalues. Alignment errors only on the HWP's result in eigenvalues in the order of $-1 \cdot 10^{-16}$ what can be considered to be in machine precision and offsets on HWP's and QWP's simultaneously produces values in the order of $-1 \cdot 10^{-2}$, so roughly an order in magnitude less than the above.

Fidelity on the other hand does severely depend on the HWP's. The smallest ones were found for $\begin{bmatrix} \alpha & 0 \\ \alpha & 0 \end{bmatrix}$ type patterns (roughly 98% for $a = \pm 2°$). If the state is a mixture, typical fidelities are in the order of $\approx 60\%$ for a mixture of $\mathcal{D}_2^1$, $\mathcal{D}_2^0$ and $\mathcal{D}_2^2$. This shows that general statements on sources for low fidelity or the occurrence of negative eigenvalues hare hard to be made, especially for larger systems where more combinations are possible.

7.4 Summary

Results in this chapter can be seen as a starting point to develop more sophisticated methods for finding alignment errors of wave plates. The used method relies on the knowledge of the real state, but this is not a good ansatz, as the calculated offsets will fit the expected counts. This is forced by the algorithm, but there is no guarantee for a connection to the real state that was measured in the setup. For example the wave plates could adapt to other alignment errors. If the 2 emission cones of the SPDC are coupled into the fiber with a different ratio, the counts will shift as well. An ideal scheme should be independent on knowledge of the state.

During alignment, the wave plates should be balanced relative to each other, that the same data will be measured for the same polarization state. In case of the 6 photonic linear setup from chapter 5.3, not only 6fold but any lower number is recorded. These events could be used to develop a scheme that allows an alignment of the wave plate relative to each other. This way, an overall offset cannot be excluded definitely, but such an alignment error will result in a global rotation of the state and this is quite easy to detect.

8 Conclusion and Outlook

In conclusion it was shown that exploiting symmetries in states can be used to reduce the effort to 3.8% compared to the generic tomographic scheme. This allowed the investigation of a 6 photonic state that would be inaccessible through the standard approach. Information about noise was preserved in the measurement and supported the expected noise model. The symmetric Dicke State was produced and observed with high accuracy while demonstrating the power of permutationally invariant quantum state tomography. Although the scheme is kept as general as possible, only a subspace of all possible density matrices is accessible; the space which fulfills the symmetry requirement.

If the observed state lies in this subspace, the scheme is equivalent to generic tomography. Another approach uses a method known as compressed sensing[19] for state tomography. This technique is originally known from signal processing and allows the guess of a signal from a certain amount of information. In state tomography, the information corresponds to local measurement settings. The expected number of sets that are needed for reliable estimation is in the same order as for permutationally invariant tomography, although slightly higher. Another benefit is that the reconstruction of the density operator already includes optimization routines. They make use of convex optimization[33] and will therefore reach the global optimum.

In the last chapter, the effect of offset in the wave plate rotations due to alignment errors is investigated. For the used 2 qubit examples, consistent results could be achieved. Performance and behaviour depends on symmetries of the observed state, because offsets can cancel out for special sign combinations. Starting with these findings, a method to investigate the linear optic setup used for 6 qubit tomography could be developed. Instead of relying on the knowledge of the ideal state, a relative scheme should be possible. Relative means that analysis blocks show offsets relative to each other rather than absolute ones to an assumed state.

Appendix A

Overlap with the symmetric subspace

In order to calculate the terms $\langle P_S^{(6)} \rangle = \mathrm{Tr}\left(P_S^{(6)}\rho\right)$ from measurements along the x,y and z-direction, one needs to decompose the operators J_i^n ($n \in \{2,4,6\}$ and $j \in \{x,y,z\}$) in terms of the tensor entries $T_{\{1,\sigma_i\}}$, where $\{1,\sigma_i\}$ is any tensor product of the unity matrix and the σ_i projector for a 6 qubit system. Those values are easily extractable from the measured data. The spin operators are defined as

$$J_i = \frac{1}{2}\sum_k \mathcal{P}_k \left(1^{\otimes N-1} \otimes \sigma_i\right)$$

The expression after the $\mathcal{P}$ stands for all permutations of $N-1$ unity matrices and one σ operator, where N is the number of qubits. A 4 qubit example reads

$$\begin{aligned} J_i &= \frac{1}{2}\left[(1\otimes 1\otimes 1\otimes \sigma_i) + (1\otimes 1\otimes \sigma_i\otimes 1) + (1\otimes \sigma_i\otimes 1\otimes 1) + (\sigma_i\otimes 1\otimes 1\otimes 1)\right] \\ &= \frac{1}{2}\left[T_{111\sigma_i} + T_{11\sigma_i 1} + T_{1\sigma_i 11} + T_{\sigma_i 111}\right] \end{aligned}$$

which is already a decomposition into the desired projectors, if the expression is put into the trace operator. Unfortunately eq. 3.9 contains terms of higher powers, which will contain cross terms. 2 properties of the components are handy:

1. The density matrices become the unity matrix if the are squared

$$\sigma_i^2 = 1$$

2. The tensor product acts on each subspace individually

$$(A_1 \otimes A_2)\cdot(B_1 \otimes B_2) = (A_1 \cdot B_1 \otimes A_2 \cdot B_2)$$

This allows easy programming by coding the position of the only Pauli Matrix in a binary number. For example only unity matrices and a single Pauli Matrix on qubit 4 can be represented by the binary number 001000. The resulting term, when multiplied with e.g. 000010 is simply the XOR operation

$$\underbrace{(1 \otimes 1 \otimes \sigma_i \otimes 1 \otimes 1 \otimes 1)}_{001000} \cdot \underbrace{(1 \otimes 1 \otimes 1 \otimes 1 \otimes \sigma_i \otimes 1)}_{000010} = \underbrace{(1 \otimes 1 \otimes \sigma_i \otimes 1 \otimes \sigma_i \otimes 1)}_{001010}$$

which leads to 001010 as the result. All that is left is to keep track on the number of terms for a certain combination. In the following, a MATLAB program for the decompositions for the terms in eq. 3.9 is listed. The output vector "counter" contains the number of terms, that are encoded in the matrix "terms". Each row is a combination, the coding is as described above. The factor $\frac{1}{2}$ in front of the sum is missing and must be accounted, when calculating the T elements from the measured data that is done in another script, implementing the patterns in chapter 3.2.

```
function [ counter, terms ] = decomposeJ( nQubits, exponent )
%DECOMPOSEJ decomposes the spin operator Ji^x into tensor terms,
%that can be extracted from measurements
%   for example the the Ji^2 for 2 qubits can be decomposed in
%   2*(1x1)+2*(sigma_i x sigma_i) which are the values of T_11
%   and T_ii beeing extractable from measurements along the i
%   direction.

% Array to keep track of the terms. Because only the position of
% the sigma matrix counts (sigma_i*sigma_i = 1), the array
% contains the number of elements with a certain position, the
% elements itself are encoded binary
counter = zeros(2^nQubits,1);
terms = zeros(2^nQubits,nQubits);

% fill the terms array (each row is one term)
for x=1:2^nQubits
 for y = 1:nQubits
  terms(x,y) = bitget(x-1,y);
 end
end

% fill the counter array with the terms in a Ji; this is
% equal to Ji^1
for x=0:nQubits-1
 counter(2^x+1) = 1;
end
% create lookup for Ji to multiply with
```

```
Ji = eye(nQubits);

% "multiply" the terms of the Ji onto the initialized
for exp=2:exponent
 % in order to multiply another J onto the existing terms, each
 % of the terms in the J, have to be multiplied by the existing
 % ones. Because sigma_i^2=1, a sigma squared at a position will
 % cancel, a sigma on a 1, will result in a sigma. Overall, just
 % the number of terms changes.
 % to prevent for double multiplication, the changes are
 % temporarily stored and later applied
 temp = zeros(2^nQubits,1);

 % iterate through the existing terms
 for exist=1:size(counter)
  if counter(exist) ~= 0

   % there is a term which can be multiplied, multiply it by each
   % term in the J, which have a sigma at each position from 1 to
   % nQubits
   for j=1:nQubits

    % Check if the term exists, if not, add 1 to the counter,
    % if it does, check to which combination it will change and
    % adjust the counters
    resulting = xor(Ji(j,:),terms(exist,:));

    % row number of resulting term
    resultingRow = bin2dec(strcat(int2str(resulting)))+1;
    temp(resultingRow) = temp(resultingRow) + counter(exist);
   end

   % delete the "original" term, the others were multiplied on
   termRow = bin2dec(strcat(int2str(terms(exist,:))))+1;
   temp(termRow) = temp(termRow) - counter(exist);
  end
 end
 % apply changes
 counter = counter + temp;
end
end
```

Appendix B

Density matrix contributions

To develop an idea how full tomography and PI tomography build up the density matrix, it is helpful to have a look at the number of elements that are summed up or subtracted at the different entries. Especially to gauge the impact of measurement errors this information is useful because elements with more contributions are likely to have smaller errors than ones with less ones. A color plot is shown in figure B.1. The statistics give

	Full Tomography	PI Tomography
Minimum	64	4
Maximum	64	63
Average	64	11.75

As expected, PI Tomography has less contributions per matrix element and instead of a homogeneous distribution patterns are visible. To develop an understanding of the error,it is not only useful to know the number of contributors, but how values are added or subtracted. If the same value is added and subtracted again that they drop out, the error becomes large.

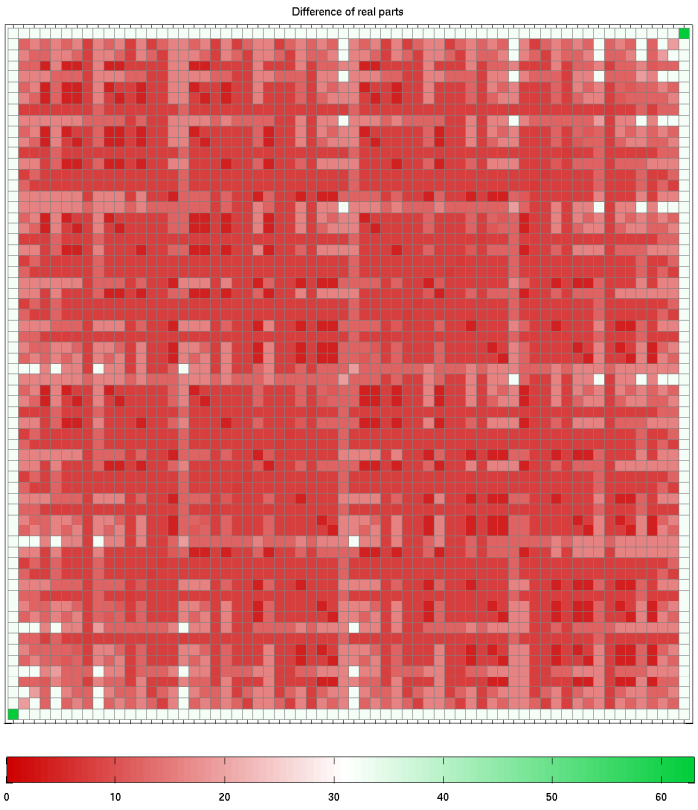

Figure B.1: Number of correlations that are summed up for individual entries in the density matrix for a 6 qubit PI tomography.

Appendix C

Counts for $|\Psi^+\rangle = \frac{1}{\sqrt{2}}(|\mathbf{HH}\rangle + |\mathbf{VV}\rangle)$

In Chapter 7 results from a 2 qubit tomography are used to extract possible offset angles for the waveplates, but do not lead to reasonable results. Here, the measured and theoretical correlations are shown. The calculated values assume an error of $\begin{bmatrix} -2 & 0 \\ 0 & 0 \end{bmatrix}$ what should correspond to the physical error as well; the reconstruction algorithm outputs $\begin{bmatrix} 2.16 & -3.20 \\ -0.17 & -4.37 \end{bmatrix}$ which are used in the "reconstructed" column. Ideal is a $|\Psi^+\rangle$ state without any error. Measured correlations are not away from the calculated, but the distance between calculated and ideal is surprisingly low. The fine discrepancies in only a few entries is absorbed by the statistical fluctuations. On the other side, entries in the reconstructed column are somewhere between measured and calculated. Distance to measured and calculated values seems low. It is important to note that for the 0° offset on all waveplates the configuration $\begin{bmatrix} 0.61 & -3.01 \\ 0.49 & -4.14 \end{bmatrix}$ was found, what might explain the angles of the quarter wave plates as a global error in addition to the artificial created.

		measured	reconstructed	calculated	ideal
XX	**HH**	0.4985	0.4895	0.5000	0.5000
	HV	0.0086	0.0105	0.0000	0
	VH	0.0099	0.0105	0.0000	0
	VV	0.4814	0.4895	0.5000	0.5000
XY	**HH**	0.2634	0.2401	0.2500	0.2500
	HV	0.2520	0.2599	0.2500	0.2500
	VH	0.2319	0.2599	0.2500	0.2500
	VV	0.2517	0.2401	0.2500	0.2500
XZ	**HH**	0.2773	0.2159	0.2506	0.2500
	HV	0.2400	0.2841	0.2494	0.2500
	VH	0.2596	0.2841	0.2494	0.2500
	VV	0.2242	0.2159	0.2506	0.2500
YX	**HH**	0.2373	0.2604	0.2500	0.2500
	HV	0.2401	0.2396	0.2500	0.2500
	VH	0.3027	0.2396	0.2500	0.2500
	VV	0.2194	0.2604	0.2500	0.2500
YY	**HH**	0.0147	0.0086	0	0
	HV	0.4685	0.4914	0.5000	0.5000
	VH	0.5066	0.4914	0.5000	0.5000
	VV	0.0107	0.0086	0	0
YZ	**HH**	0.2659	0.2911	0.2500	0.2500
	HV	0.2153	0.2089	0.2500	0.2500
	VH	0.2569	0.2089	0.2500	0.2500
	VV	0.2614	0.2911	0.2500	0.2500
ZX	**HH**	0.2764	0.2756	0.2494	0.2500
	HV	0.2259	0.2244	0.2506	0.2500
	VH	0.2664	0.2244	0.2506	0.2500
	VV	0.2321	0.2756	0.2494	0.2500
ZY	**HH**	0.2883	0.2730	0.2500	0.2500
	HV	0.2187	0.2270	0.2500	0.2500
	VH	0.2063	0.2270	0.2500	0.2500
	VV	0.2880	0.2730	0.2500	0.2500
ZZ	**HH**	0.4932	0.4895	0.5000	0.5000
	HV	0.0025	0.0105	0	0
	VH	0.0041	0.0105	0	0
	VV	0.4991	0.4895	0.5000	0.5000

Appendix D

Symmetries

In chapter 7, it was found that symmetric errors in the position of the HWP's and QWP can cancel out.

D.1 The 2 qubit symmetric Dicke State

The results from the simulations suggest that errors on the HWP's on qubit 1 and 2 can cancel out. The density matrix for $\mathcal{D}_2^1$ reads

$$|\mathcal{D}_2^1\rangle = \frac{1}{\sqrt{2}}\left(|\mathrm{HV}\rangle + |\mathrm{VH}\rangle\right) \Rightarrow \rho_{\mathcal{D}_2^1} = \frac{1}{2}\begin{pmatrix} 0 & 0 & 0 & 0 \\ 0 & 1 & 1 & 0 \\ 0 & 1 & 1 & 0 \\ 0 & 0 & 0 & 0 \end{pmatrix}$$

Rotations of the state by the 2 HWP's is done via the operator

$$\mathcal{O}(\alpha, \beta) = \mathrm{HWP}(\alpha) \otimes \mathrm{HWP}(\beta)$$

for the operations to cancel

$$\mathcal{O}(\alpha, \beta)\, \rho_{\mathcal{D}_2^1} \mathcal{O}(\alpha, \beta)^\dagger = \rho_{\mathcal{D}_2^1}$$

must hold. With $\gamma = 2\alpha + 2\beta$

$$\mathcal{O}(\alpha, \beta)\, \rho_{\mathcal{D}_2^1} \mathcal{O}(\alpha, \beta)^\dagger = \frac{1}{2}\begin{pmatrix} \sin(\gamma)^2 & -\sin(\gamma)\cos(\gamma) & -\sin(\gamma)\cos(\gamma) & -\sin(\gamma)^2 \\ -\sin(\gamma)\cos(\gamma) & \cos(\gamma)^2 & \cos(\gamma)^2 & \cos(\gamma)\sin(\gamma) \\ -\sin(\gamma)\cos(\gamma) & \cos(\gamma)^2 & \cos(\gamma)^2 & \cos(\gamma)\sin(\gamma) \\ -\sin(\gamma)^2 & \cos(\gamma)\sin(\gamma) & \cos(\gamma)\sin(\gamma) & \sin(\gamma)^2 \end{pmatrix}$$

and therefore $\cos(\gamma) \stackrel{!}{=} 1$ and any $\sin(\gamma) \stackrel{!}{=} 0$ what is true for $\alpha = -\beta$. The interpretation is that opposite offsets on the HWP's cancel out what can be seen in some reconstruction simulation where arbitrary but opposite offsets are found for no assumed error on the HWP's. For QWP's or any combination with HWP's, no relation between α and β can be found to fulfill similar symmetry.

For the 6 photon symmetric Dicke State, no such symmetry was found.

D.2 The Bell States

The initial symmetry was found using numerical calculations, here the resulting angle errors that lead to a fidelity of 1 on the Bell states are listed. The convention for the errors is

$$\begin{array}{c} \\ \text{Qubit 1} \\ \text{Qubit 2} \end{array} \begin{array}{c} \begin{array}{cc} \text{HWP} & \text{QWP} \end{array} \\ \begin{bmatrix} \text{offset angle}[^\circ] & \text{offset angle}[^\circ] \\ \text{offset angle}[^\circ] & \text{offset angle}[^\circ] \end{bmatrix} \end{array} \tag{D.1}$$

$|\Phi^+\rangle = \frac{1}{\sqrt{2}}(|00\rangle + |11\rangle)$

$$\begin{bmatrix} \alpha & 0 \\ \alpha & 0 \end{bmatrix}$$

$|\Phi^-\rangle = \frac{1}{\sqrt{2}}(|00\rangle - |11\rangle)$

$$\begin{bmatrix} \alpha & 0 \\ -\alpha & 0 \end{bmatrix}$$

$|\Psi^+\rangle = \frac{1}{\sqrt{2}}(|10\rangle + |01\rangle)$

$$\begin{bmatrix} \alpha & 0 \\ -\alpha & 0 \end{bmatrix}$$

$|\Psi^-\rangle = \frac{1}{\sqrt{2}}(|10\rangle - |01\rangle)$

$$\begin{bmatrix} \alpha & 0 \\ \alpha & 0 \end{bmatrix} \text{ and } \begin{bmatrix} 0 & \alpha \\ 0 & \alpha \end{bmatrix}$$

The easiest way to quickly check the effect of any additional offset is to calculate the commutator of the density operator with the offset operator.

Appendix E

Additional simulation results

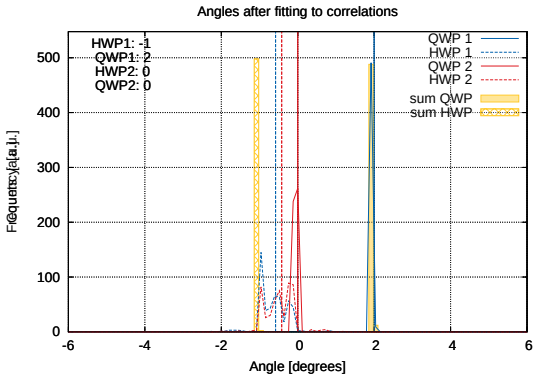

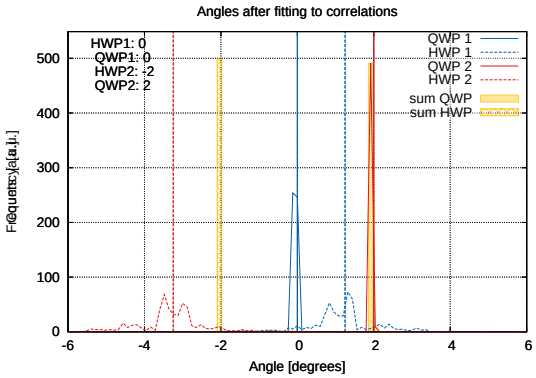

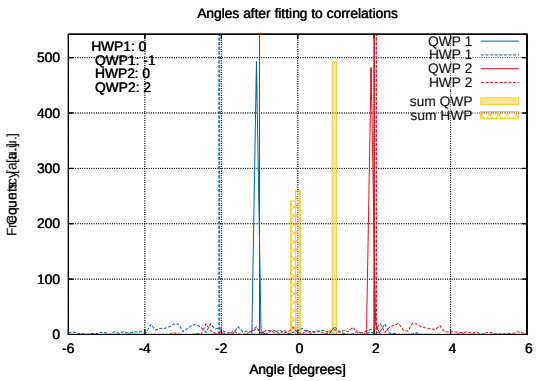

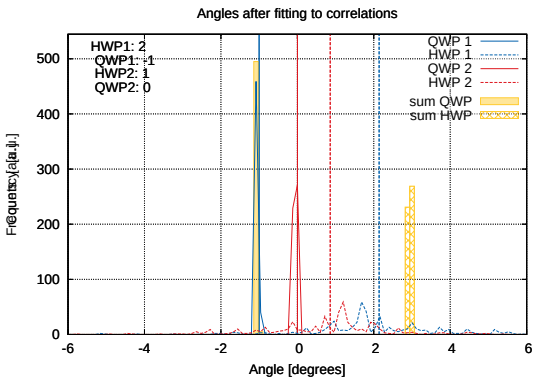

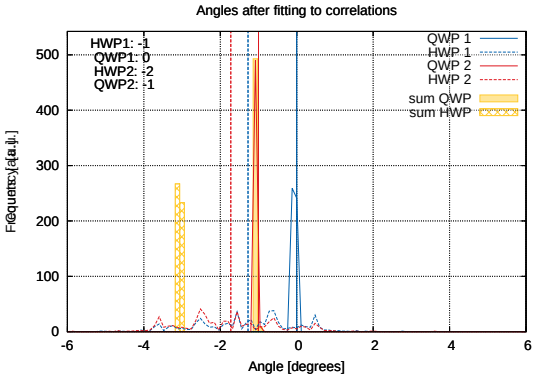
Angles after fitting to correlations
HWP1: -1
QWP1: 0
HWP2: -2
QWP2: -1
QWP 1
HWP 1
QWP 2
HWP 2
sum QWP
sum HWP
Angle [degrees]

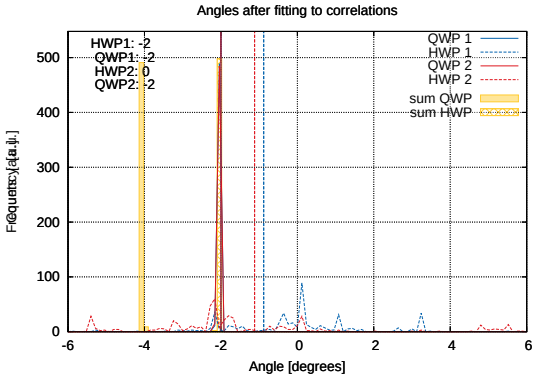
Angles after fitting to correlations
HWP1: -2
QWP1: -2
HWP2: 0
QWP2: -2
QWP 1
HWP 1
QWP 2
HWP 2
sum QWP
sum HWP
Angle [degrees]

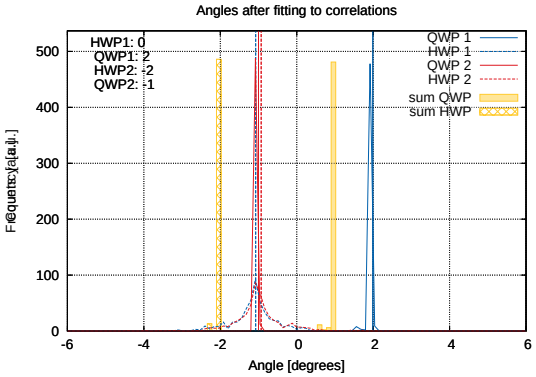
Angles after fitting to correlations
HWP1: 0
QWP1: 2
HWP2: -2
QWP2: -1
QWP 1
HWP 1
QWP 2
HWP 2
sum QWP
sum HWP
Angle [degrees]

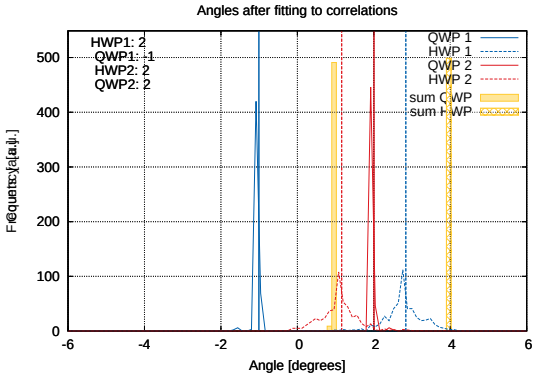
Angles after fitting to correlations
HWP1: 2
QWP1: -1
HWP2: 2
QWP2: 2
QWP 1
HWP 1
QWP 2
HWP 2
sum QWP
sum HWP
Angle [degrees]

Appendix F

Additional density matrices

For comparison, an ideal and ideal noisy ($p = 0.3$) $\mathcal{D}_6^3$ state are plotted as a 3 dimensional bar chart. The imaginary parts are always zero, the noise is visible in a decrease of amplitude of the entries that are present without noise and an additional plateau.

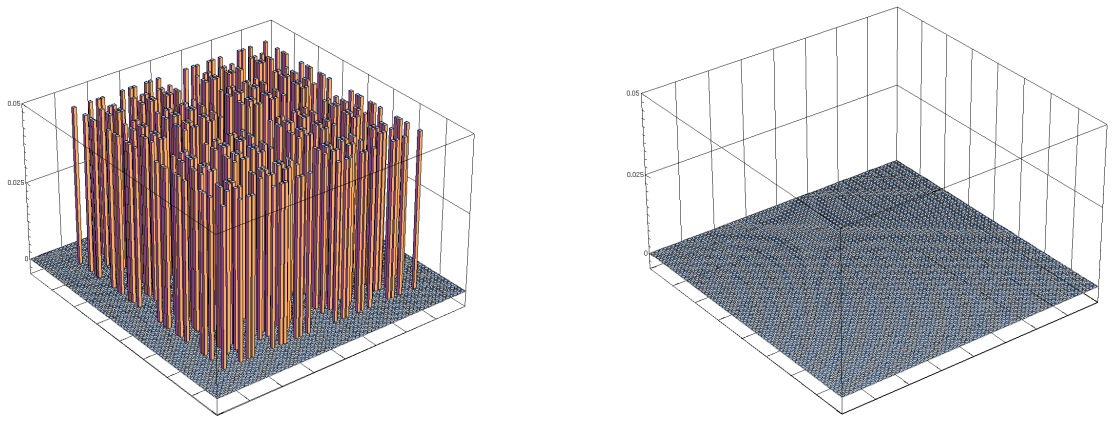

(a) Real part

(b) Imaginary part

Figure F.1: Real and imaginary part of an ideal $\mathcal{D}_6^3$ state

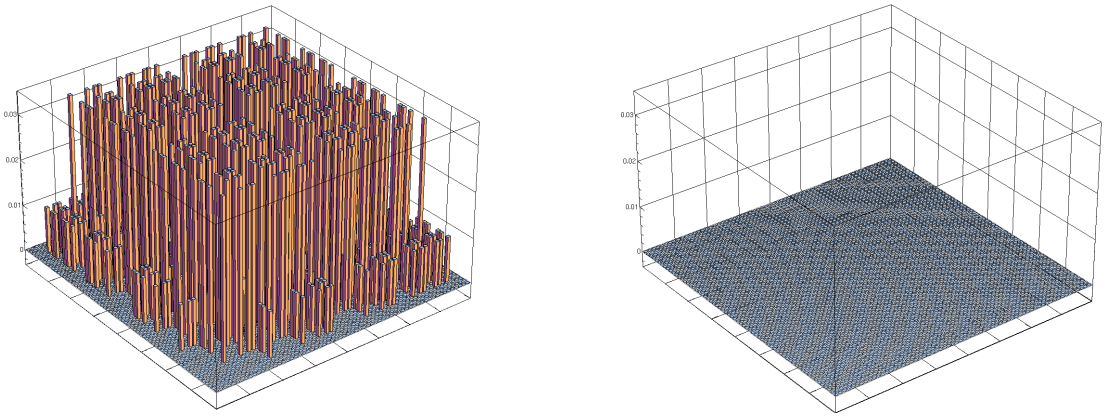

(a) Real part (b) Imaginary part

Figure F.2: Real and imaginary part of an ideal noisy $\mathcal{D}_6^3$ state for $p = 0.3$

Bibliography

[1] F. Bloch. Nuclear induction. *Phys. Rev.*, 70:460–474, Oct 1946.

[2] Robin Blume-Kohout. Hedged maximum likelihood quantum state estimation. *Phys. Rev. Lett.*, 105:200504, Nov 2010.

[3] Robin Blume-Kohout. Optimal, reliable estimation of quantum states. *New Journal of Physics*, 12(4):043034, 2010.

[4] Max Born. *Principles of Optics-7th ed.* Cambridge University Press, 1999.

[5] Agedi N. Boto, Pieter Kok, Daniel S. Abrams, Samuel L. Braunstein, Colin P. Williams, and Jonathan P. Dowling. Quantum interferometric optical lithography: Exploiting entanglement to beat the diffraction limit. *Phys. Rev. Lett.*, 85:2733–2736, Sep 2000.

[6] Stephen Boyd and Lieven Vandenberghe. *Convex Optimization*. Cambridge University Press, 2004.

[7] Julia Buluta, Sahel Ashhab, and Franco Noir. Natural and artificial atoms for quantum computation. *Rep. Prog. Phys*, 74:104404, 2011.

[8] Donald Bures. An extension of kakutani's theorem on infinite product measures ot the tensor produt of semifinite w* algebras. *Transactions of the American Mathematical Society*, 135:199–212, 1969.

[9] R. L. Byer and S. E. Harris. Power and bandwidth of spontaneous parametric emission. *Phys. Rev.*, 168:1064–1068, Apr 1968.

[10] J. I. Cirac, A. K. Ekert, and C. Macchiavello. Optimal purification of single qubits. *Phys. Rev. Lett.*, 82(21):4344–4347, May 1999.

[11] R. H. Dicke. Coherence in spontaneous radiation processes. *Phys. Rev.*, 93(1):99, Jan 1954.

[12] Paul A. M. Dirac. *The principles of quantum mechanics.* Oxford, Clarendon Press, 2003.

[13] W. Dür, G. Vidal, and J. I. Cirac. Three qubits can be entangled in two inequivalent ways. *Phys. Rev. A*, 62:062314, Nov 2000.

[14] A. Einstein, B. Podolsky, and N. Rosen. Can quantum-mechanical description of physical reality be considered complete? *Phys. Rev.*, 47:777–780, May 1935.

[15] H. S. Eisenberg, G. Khoury, G. A. Durkin, C. Simon, and D. Bouwmeester. Quantum entanglement of a large number of photons. *Phys. Rev. Lett.*, 93(19):193901, Nov 2004.

[16] Christopher A. Fuchs and Jeroen van de Graaf. Cryptographic distinguishability measures for quantum mechanical states. 2007.

[17] Otfried Gühne and Geza Toth. Entanglement detection. *Physics Reports*, 474,:1, November 2008.

[18] David J. Griffiths. *Introduction to Quantum Mechanics*. Pearson Prentice Hall, 2005.

[19] David Gross, Yi-Kai Liu, Steven T. Flammia, Stephen Becker, and Jens Eisert. Quantum state tomography via compressed sensing. *Phys. Rev. Lett.*, 105,:150401, September 2009.

[20] T.W. Hansch and B. Couillaud. Laser frequency stabilization by polarization spectroscopy of a reflecting reference cavity. *Optics Communications*, 35(3):441 – 444, 1980.

[21] Z. Hradil. Quantum-state estimation. *Phys. Rev. A*, 55:R1561–R1564, Mar 1997.

[22] Daniel F. V. James, Paul G. Kwiat, William J. Munro, and Andrew G. White. Measurement of qubits. *Phys. Rev. A*, 64(5):052312, Oct 2001.

[23] Brian Julsgaard, Alexander Kozhekin, and Eugene S. Polzik. Experimental long-lived entanglement of two macroscopic objects. *Nature*, 413(6854):400–403, September 2001.

[24] Timothy E. Keller and Morton H. Rubin. Theory of two-photon entanglement for spontaneous parametric down-conversion driven by a narrow pump pulse. *Phys. Rev. A*, 56:1534–1541, Aug 1997.

[25] N. Kiesel, C. Schmid, G. Tóth, E. Solano, and H. Weinfurter. Experimental observation of four-photon entangled dicke state with high fidelity. *Phys. Rev. Lett.*, 98(6):063604, Feb 2007.

[26] D. Klinger and J. Lewis, editors. *Polarized light in optics and spectroscopy*. Academic Press, 1990.

[27] Roland Krischek, Christian Schwemmer, Witlef Wieczorek, Harald Weinfurter, Philipp Hyllus, Luca Pezzé, and Augusto Smerzi. Useful multiparticle entanglement and sub-shot-noise sensitivity in experimental phase estimation. *Phys. Rev. Lett.*, 107:080504, Aug 2011.

[28] Roland Krischek, Witlef Wieczorek, Akira Ozawa, Nikolai Kiesel, Patrick Michelberger, Thomas Udem, and Harald Weinfurter. Ultraviolet enhancement cavity for ultrafast nonlinear optics and high-rate multiphoton entanglement experiments. *Nat Photon*, 4(3):170–173, March 2010.

[29] Douglas Magde and Herbert Mahr. Study in ammonium dihydrogen phosphate of spontaneous parametric interaction tunable from 4400 to 16 000 å. *Phys. Rev. Lett.*, 18:905–907, May 1967.

[30] Harold Metcalf. Magneto-optical trapping and its application to helium metastables. *J. Opt. Soc. Am. B*, 6(11):2206–2210, Nov 1989.

[31] M.G.A Paris and J Rehacek, editors. *Quantum State Estimation*. Springer, 2004.

[32] G. J. Pryde, J. L. O'Brien, A. G. White, S. D. Bartlett, and T. C. Ralph. Measuring a photonic qubit without destroying it. *Phys. Rev. Lett.*, 92:190402, May 2004.

[33] Michael Reimpell. *Quantum Information and Convex Optimization*. PhD thesis, Technische Universität Carolo-Wilhelmina, 2008.

[34] Jun J. Sakurai. *Modern Quantum Mechanics*. Addison-Wesley, 2005.

[35] B.A.E. Saleh and M.C. Teich. *Fundamentals of Photonics*. J. Wiley & Sons, 1991.

[36] Marek Sasura and Vladimír Buzek. Cold trapped ions as quantum information processors. *Journal of Modern Optics*, 49(10):1593 – 1647, 2002.

[37] Benjamin Schumacher. Quantum coding. *Phys. Rev. A*, 51:2738–2747, Apr 1995.

[38] Franz Schwabel. *Quantum Mechanics*. Springer, 2007.

[39] John K. Stockton, J. M. Geremia, Andrew C. Doherty, and Hideo Mabuchi. Characterizing the entanglement of symmetric many-particle spin-$\frac{1}{2}$ systems. *Phys. Rev. A*, 67(2):022112, Feb 2003.

[40] G. Toth, W. Wieczorek, D. Gross, R. Krischek, C. Schwemmer, and H. Weinfurter. Permutationally invariant quantum tomography. *Phys. Rev. Lett.*, 105(25):250403, Dec 2010.

[41] G. Toth, W. Wieczorek, D. Gross, R. Krischek, C. Schwemmer, and H. Weinfurter. Permutationally invariant quantum tomography (supplement). *Phys. Rev. Lett.*, 105(25):250403, Dec 2010.

[42] Geza Toth. Detection of multipartite entanglement in the vicinity of symmetric dicke states. *J. Opt. Soc. Am. B*, 24,:275, 2007.

[43] Pavel Trojek. *Efficient Generation of Photonic Entanglement and Multiparty Quatum Communication.* PhD thesis, Ludwig Maximilians Universität München, 2007.

[44] J. von Neumann. Mathematische begründung der quantenmechanik. *Nachrichten von der Gesellschaft der Wissenschaften zu Göttingen, Mathematisch-Physikalische Klasse*, 1927.

[45] Reinhard F. Werner. Quantum states with einstein-podolsky-rosen correlations admitting a hidden-variable model. *Phys. Rev. A*, 40:4277–4281, Oct 1989.

[46] Witlef Wieczorek. *Multi-Photon Entanglement: Experimental Observation, Characterization, and Application of up to Six-Photon Entangled States.* PhD thesis, Ludwig Maximilians Universität München, 2009.

[47] Xing-Can Yao, Tian-Xiong Wang, Ping Xu, He Lu, Ge-Sheng Pan, Xiao-Hui Bao, Cheng-Zhi Peng, Chao-Yang Lu, Yu-Ao Chen, and Jian-Wei Pan. Observation of eight-photon entanglement. May 2011.

Erklärung:

Hiermit erkläre ich, die vorliegende Arbeit selbständig verfasst zu haben und keine anderen als die in der Arbeit angegebnene Quellen und Hilfsmittel benutzt zu haben.

München den 27.10.2011